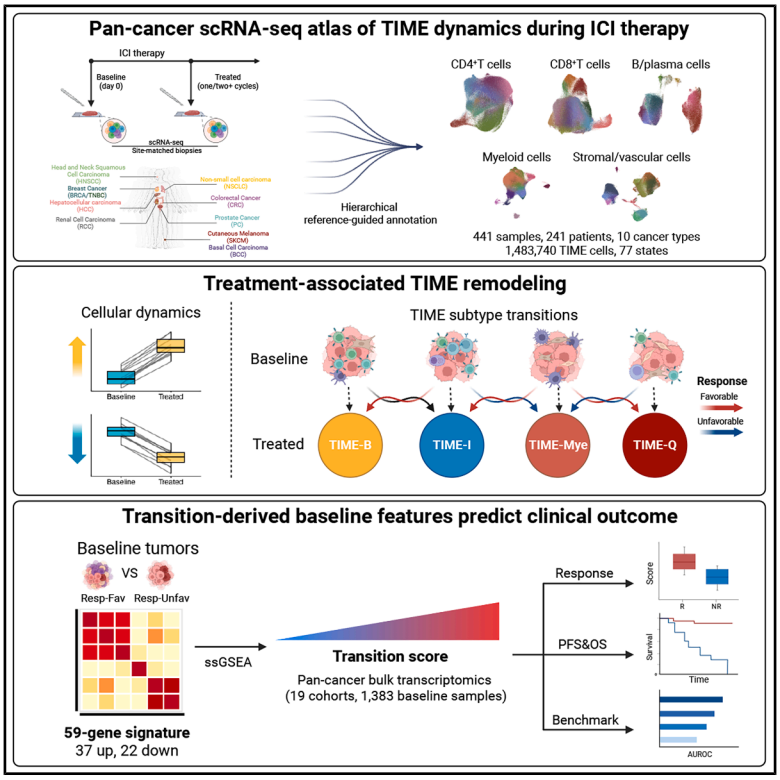
Cancer Cell

Article

Tumor immune microenvironment remodeling predicts response to checkpoint inhibitor therapy

Graphical abstract



Highlights

- A longitudinal pan-cancer atlas maps tumor immune microenvironment (TIME) remodeling
- Four conserved TIME states recur across cancer types
- TIME transitions during therapy track response better than the baseline state
- A transition-derived baseline signature predicts response and survival

Authors

Zhongyang Lin, Mitalee Chandra, Nalini Srinivas, Selma Ugurel, Jürgen C. Becker, Dvir Aran

Correspondence

j.becker@dkfz-heidelberg.de (J.C.B.), dviraran@technion.ac.il (D.A.)

In brief

Lin et al. assemble a longitudinal pan-cancer single-cell atlas that tracks how the tumor immune microenvironment remodels during checkpoint inhibitor therapy. They show that the direction of remodeling, rather than the pre-treatment state, predicts response and translate these dynamics into a baseline gene signature that forecasts outcome across cancer types.

Lin et al., 2026, Cancer Cell *44*, 1–15
September 14, 2026 © 2026 Elsevier Inc. All rights reserved, including those for text and data mining, AI training, and similar technologies.
https://doi.org/10.1016/j.ccell.2026.08.007

CellPress

Please cite this article in press as: Lin et al., Tumor immune microenvironment remodeling predicts response to checkpoint inhibitor therapy, Cancer Cell (2026), https://doi.org/10.1016/j.ccell.2026.08.007

Cancer Cell

CellPress

Article

Tumor immune microenvironment remodeling predicts response to checkpoint inhibitor therapy

Zhongyang Lin,[1] Mitalee Chandra,[2,3] Nalini Srinivas,[2,3,4] Selma Ugurel,[3,4] Jürgen C. Becker,[2,3,4,*] and Dvir Aran[1,5,6,*]
[1]Faculty of Biology, Technion-Israel Institute of Technology, Haifa, Israel
[2]Translational Skin Cancer Research, German Cancer Consortium (DKTK), Partner Site Essen, Medical Faculty, University of Duisburg-Essen, Essen, Germany
[3]German Cancer Consortium (DKTK), German Cancer Research Center (DKFZ), Heidelberg, Germany
[4]Department of Dermatology, University Hospital Essen, Essen, Germany
[5]The Taub Faculty of Computer Science, Technion-Israel Institute of Technology, Haifa, Israel
[6]Lead contact
*Correspondence: j.becker@dkfz-heidelberg.de (J.C.B.), dviraran@technion.ac.il (D.A.)
https://doi.org/10.1016/j.ccell.2026.08.007

SUMMARY

Immune checkpoint inhibitors (ICIs) have transformed cancer therapy, yet the basis of variable patient responses remains unclear. We assemble a longitudinal single-cell RNA sequencing atlas of 441 samples from 241 patients across ten cancer entities to map treatment-associated remodeling of the tumor immune microenvironment (TIME). With a hierarchical reference-guided deep-phenotyping framework, we define 77 immune and stromal subtypes and resolve four conserved TIME subtypes. Approximately 40% of tumors shift between states during therapy, and the transition is more predictive of outcome than the baseline state. Favorable transitions toward inflamed or B cell-enriched subtype track with improved response and survival, while persistence in or shifts toward myeloid dominance indicate resistance. We derive a 59-gene signature that predicted response and survival for 1,383 baseline tumors across 19 independent cohorts. These findings establish immunotype transitions as a central determinant of ICI efficacy, offering new avenues for response prediction and rational immunotherapy design.

INTRODUCTION

Immune checkpoint inhibitors (ICIs) have transformed cancer therapy by reinvigoration of anti-tumor immunity, achieving durable responses in patients with previously intractable malignancies.[1–4] Thus, ICIs have become standard-of-care for many cancer types. Despite the successes, however, more than half of patients either fail to respond initially or develop acquired resistance. This notion has driven an intense search for biomarkers to improve response prediction and allow personalized therapeutic strategies to overcome resistance.

The tumor immune microenvironment (TIME) critically impacts the outcome of anti-tumor immune responses.[5,6] Tumors are often described along a hot-to-cold spectrum that reflects the distribution and functional state of immune cells within and around the tumor. Hot tumors typically show cytotoxic T cells, interferon signaling, and antigen presentation features and tend to respond better.[7] Cold tumors tend to be T cell deficient or T cell excluded and are often dominated by suppressive myeloid and regulatory programs that resist activation.[8] These patterns have been observed with bulk expression, spatial assays, and single-cell profiling and have anchored many current predictors,[9–13] yet this framework implicitly treats the TIME as a fixed, pre-treatment attribute of the tumor. Checkpoint blockade, however, is not a passive test of immune readiness but a potent perturbation that can rewire the cellular composition and function. An overly simplistic assumption could obscure the fact that ICIs act as a profound intervention that actively reshapes TIME by reactivating lymphocytes and altering myeloid populations. Early on-treatment molecular remodeling, including T cell reinvigoration, B cell activation, and clonal expansion, has been shown to correlate with clinical benefit.[14–17] Recognizing the TIME as a dynamic system rather than a static trait reframes the question from whether a tumor is hot or cold to how its immune ecosystem evolves once therapy begins and whether those trajectories can predict outcome.[18]

Testing this hypothesis requires longitudinal sampling of tumors before and during therapy, enabling direct observation of TIME remodeling and its link to treatment efficacy. Analyses on consecutively sampled tumors have provided unprecedented insights into TIME dynamics in easy-to-biopsy cancers[15,16,19]; this approach has been expanded to include the neoadjuvant therapy setting, which allows for the collection of sequential tumor samples.[20–30] Nonetheless, investigating TIME dynamics has faced several challenges. For example, studies examining treatment-associated compositional shifts typically include 10–20 patients with paired samples, lacking sufficient statistical power to detect subtle but clinically relevant features. Comparing data across different studies is hampered by batch effects and methodology inconsistencies, such as cell annotation and compositional

All rights are reserved, including those for text and data mining, AI training, and similar technologies.

Please cite this article in press as: Lin et al., Tumor immune microenvironment remodeling predicts response to checkpoint inhibitor therapy, Cancer Cell (2026), https://doi.org/10.1016/j.ccell.2026.08.007

analysis. Thus, although the TIME cell lineages and classifications have been extensively explored,[9,10,31–38] the full plot of TIME dynamics and the association with treatment efficacy remain poorly characterized. Overcoming these barriers to data integration will be crucial to unlocking the potential of pan-cancer meta-analyses to address these gaps.

Here, we address this gap by assembling large-scale longitudinal single-cell RNA sequencing (scRNA-seq) compendium of ICI-treated tumors to date, encompassing 441 samples from 241 patients across 10 cancer types. To overcome the challenges of cross-cohort integration, we developed a hierarchical, reference-guided, deep-phenotyping framework that enables consistent cell-type classification and compositional analysis across studies. This approach allowed us to define a compact and reproducible set of TIME states and to track transitions in paired pre- and on-treatment samples. We hypothesized that the direction of TIME remodeling during ICI therapy is associated with clinical outcome and that the baseline molecular programs determine each tumor's propensity for favorable or unfavorable evolution. By mapping these dynamics across cancer types, we reveal conserved trajectories of immune remodeling that link early cellular plasticity to therapeutic efficacy. This work extends prior studies by providing a unified, longitudinal framework to assess how TIME remodeling, beyond its baseline composition, relates to immunotherapy response.

RESULTS

Pan-cancer atlas reveals landscape of TIME dynamics

To systematically investigate cellular remodeling under ICI therapy, we first generated scRNA-seq data from paired tumor biopsies of 17 cutaneous melanoma (SKCM) patients collected at treatment initiation (day 0) and 6–16 days after anti-PD-1 ± anti-CTLA-4 therapy initiation, capturing early treatment-associated changes (Table S1). We further assembled a pan-cancer atlas by integrating sequential scRNA-seq datasets from 15 independent studies encompassing 10 cancer types. A key feature of this atlas is the inclusion of consecutively sampled, site-matched tumors from ICI-treated patients, covering additional SKCM as well as a diverse range of malignancies: head and neck squamous cell carcinoma (HNSCC), non-small cell lung cancer (NSCLC), ER/HER2/PR ± breast cancer (BRCA), triple-negative breast cancer (TNBC), hepatocellular carcinoma (HCC), colorectal cancer (CRC), prostate cancer (PC), and basal cell carcinoma (BCC) (Figures 1A–1C; Table S2). Importantly, these cohorts span a range of treatment durations, from within the first cycle through two cycles and up to four completed cycles, enabling a systematic comparison of TIME dynamics along the treatment course (Figure S1A). After rigorous quality control, the atlas comprised 1,483,740 TIME cells derived from 370 samples with complete profiling and 71 samples from $CD45^+$ sorted cells.

We applied a hierarchical reference-guided deep-phenotyping framework to assign cell identities at multiple resolutions. In the first step, each dataset was independently annotated with SingleR, supplemented by scGate filtering and Seurat clustering, to resolve ambiguous populations.[39,40] These preliminary labels were then iteratively refined throughout the annotation: misclassified clusters were corrected based on marker expression, and potential doublets were removed (STAR Methods). Finally, we performed cross-dataset integration within each major lineage to harmonize labels and ensure consistency across cohorts (STAR Methods; Figures 1B and S1B–S1D). Canonical marker gene expression confirmed accurate classification of 11 distinct cell types across all datasets (Figures 1D and S1E).

To investigate treatment-associated changes in cell composition, we performed a cross-cohort meta-analysis of baseline and on-treatment samples (STAR Methods). This analysis revealed a consistent enrichment of monocytes/macrophages (mono/macro) paralleled by a distinct reduction in malignant cells upon ICI therapy (Figure 1E). These compositional trends were recurrent across studies and correlated with standardized binary response metrics (Figures S1F and S1G). To ensure these compositional trends were not confounded by the inherent constraints of proportional data, we applied scCODA as an orthogonal validation.[41] The scCODA-derived posterior effects showed broad concordance with our Wilcoxon-based meta-analysis estimates ($r = 0.66$, $p = 0.006$; Figure S1H), though NK cells and conventional dendritic cells (cDCs)—two sparse cell populations previously implicated in ICI response[42]—showed discordant directions between the two approaches, which warrant further investigation. Beyond these global patterns, cancer-type-specific dynamics emerged. For instance, B cell infiltration increased in BCC, BRCA, and HNSCC, whereas plasma cells were mainly accumulated in baseline, particularly in NSCLC patients receiving anti-PD1 therapy combined with chemotherapy (Figure S1I). Subgroup analyses further refined these observations: in ER^+ BRCA, a single cycle of anti-PD1 therapy increased myeloid cell infiltration, whereas in TNBC, it increased cycling T/NK cells and reduced mast cells (Figure S1J). When stratified by T cell expansion, patients with expansion displayed elevated plasmacytoid dendritic cells (pDCs) and B cells, while those without expansion had increased monocytes/macrophages and fewer $CD8^+$ T cells; mast cell depletion was also observed in responders by Response Evaluation Criteria in Solid Tumors (RECIST; Figure S1K). In HNSCC, combination therapy showed a more uniform pattern, with the accumulation of B cells, plasma cells, and mast cells within two weeks, whereas after two cycles (approximately 3–4 weeks), there was a significant reduction in pDCs and cDCs (Figure S1L). Although these early compositional shifts were not significantly linked to T cell expansion or short-term clinical response, they indicate that ICIs induce widespread, multi-lineage remodeling of the tumor microenvironment (TME) extending well beyond T cell reactivation.

High-resolution immune cell mapping uncovers treatment- and response-linked TIME shifts

In the second step of our deep-phenotyping framework, we applied lineage-specific reference panels derived from curated pan-cancer single-cell atlases to resolve fine-grained immune and stromal subtypes within each lineage (STAR Methods; Figures S1B and 2A). This hierarchical approach allowed accurate discrimination of the overlapping populations such as T, NK, and myeloid subsets while controlling for technical and study-specific biases (Figure 2B). The annotation framework identified 62 immune and 15 non-immune cell subtypes (Table S3). The assignment was confirmed by both marker gene expression and functional enrichment analysis with curated signatures, consistent with prior studies (Figures S2A–S2L).[33,37,43–46]

Please cite this article in press as: Lin et al., Tumor immune microenvironment remodeling predicts response to checkpoint inhibitor therapy, Cancer Cell (2026), https://doi.org/10.1016/j.ccell.2026.08.007

CellPress

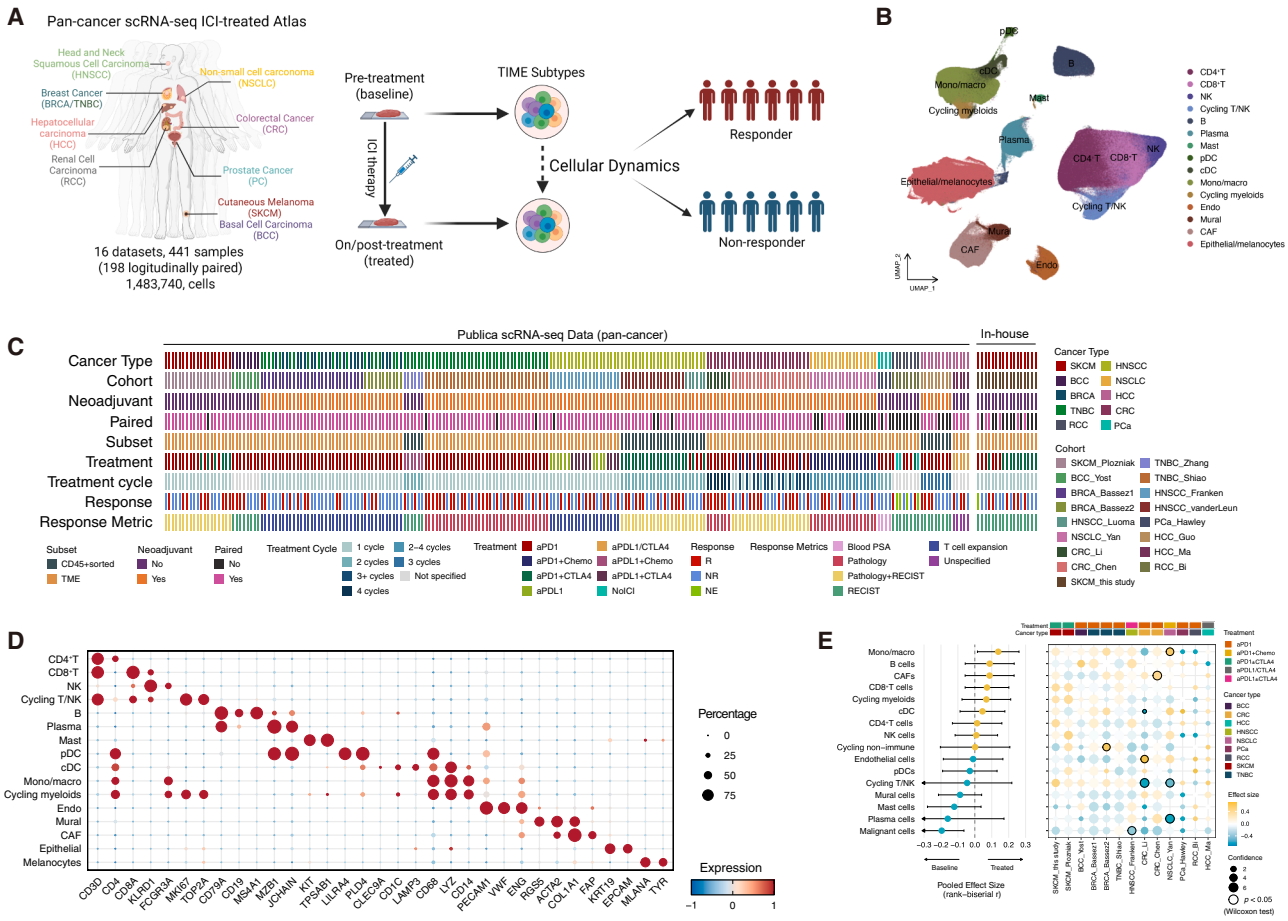


Figure 1. Construction and composition of the longitudinal single-cell atlas of ICI-treated tumors

(A) Schematic overview of the study design and analytical workflow, illustrating the integration of longitudinal scRNA-seq datasets from multiple cancer types and mapping of tumor immune microenvironment (TIME) dynamics between pre- and on-treatment samples.

(B) Uniform manifold approximation and projection (UMAP) of the integrated dataset, showing major immune and stromal lineages across all samples.

(C) Summary of included studies and metadata, indicating cohort origin, cancer type, treatment regimen, sampling interval, and availability of paired and response information. Publicly available patients, $n = 228$; in-house SKCM patients, $n = 17$.

(D) Validation of main cell type assignments, with canonical marker gene expression confirming accurate classification of eleven distinct cell lineages.

(E) Meta-analysis of compositional shifts during ICI therapy, showing study-specific estimates (dot plot) and pooled effect sizes (forest plot) for each major cell type. In the dot plot, colors show effect size (rank-biserial correlation) of cell types for each cohort, and dot size reflects the confidence of each estimate (inverse of the standard error). The forest plot displays the pooled effect size estimated by a random-effects meta-analysis with restricted maximum likelihood (REML), with 95% confidence intervals indicated by error bars. Statistical significance was assessed with unpaired two-sided Wilcoxon rank-sum test. Baseline $n = 182$; Treated $n = 192$.

See also Figure S1 and Tables S1 and S2.

To characterize treatment-associated dynamics at subtype resolution, we performed paired Wilcoxon rank-sum test within each cohort followed by random-effects meta-analysis comparing baseline and treated samples (Figure 2C; Table S4). Several cell types showed recurrent enrichment across all time points, including follicular helper T cells (CD4_Tfh), *GZMK*$^+$ cytotoxic CD8$^+$ T cells (CD8_Tex_GZMK), cycling germinal center B cells, and *TREM2*$^+$ macrophages, while interferon-stimulated gene-expressing T cells (CD4_T-ISG and CD8_T-ISG) and pericytes were consistently decreased (Table S4). The overlay revealed that these recurrent changes had distinct temporal profiles (Figure 2C; Table S4). CD4_Tfh enrichment peaked after a single cycle then attenuated, suggesting rapid early mobilization, and CD8_Tex_GZMK enrichment was similarly concentrated at early time points. In contrast, regulatory T cells (CD4_Treg) showed no significant change after one cycle but decreased substantially after extended treatment. Pericytes, myofibroblasts, and desmoplastic cancer-associated fibroblasts (CAFs) showed significant depletion after two or more cycles, especially in CRC (Figure 2C; Table S4). Per-patient fold-change tracking across cancer types confirmed that CD4_Tfh enrichment and T-ISG decline were concordant across most tumor types, whereas other dynamics, notably ISG-expressing macrophages (Macro-ISG) and CD4_Treg, displayed heterogeneous, cancer-type-dependent trajectories (Figure 2D).

In response-stratified analysis, we observed that T-ISG and ISG-expressing B cell (B-ISG) depletion was shared at one cycle but intensified selectively in responders at later cycles, whereas

Please cite this article in press as: Lin et al., Tumor immune microenvironment remodeling predicts response to checkpoint inhibitor therapy, Cancer Cell (2026), https://doi.org/10.1016/j.ccell.2026.08.007

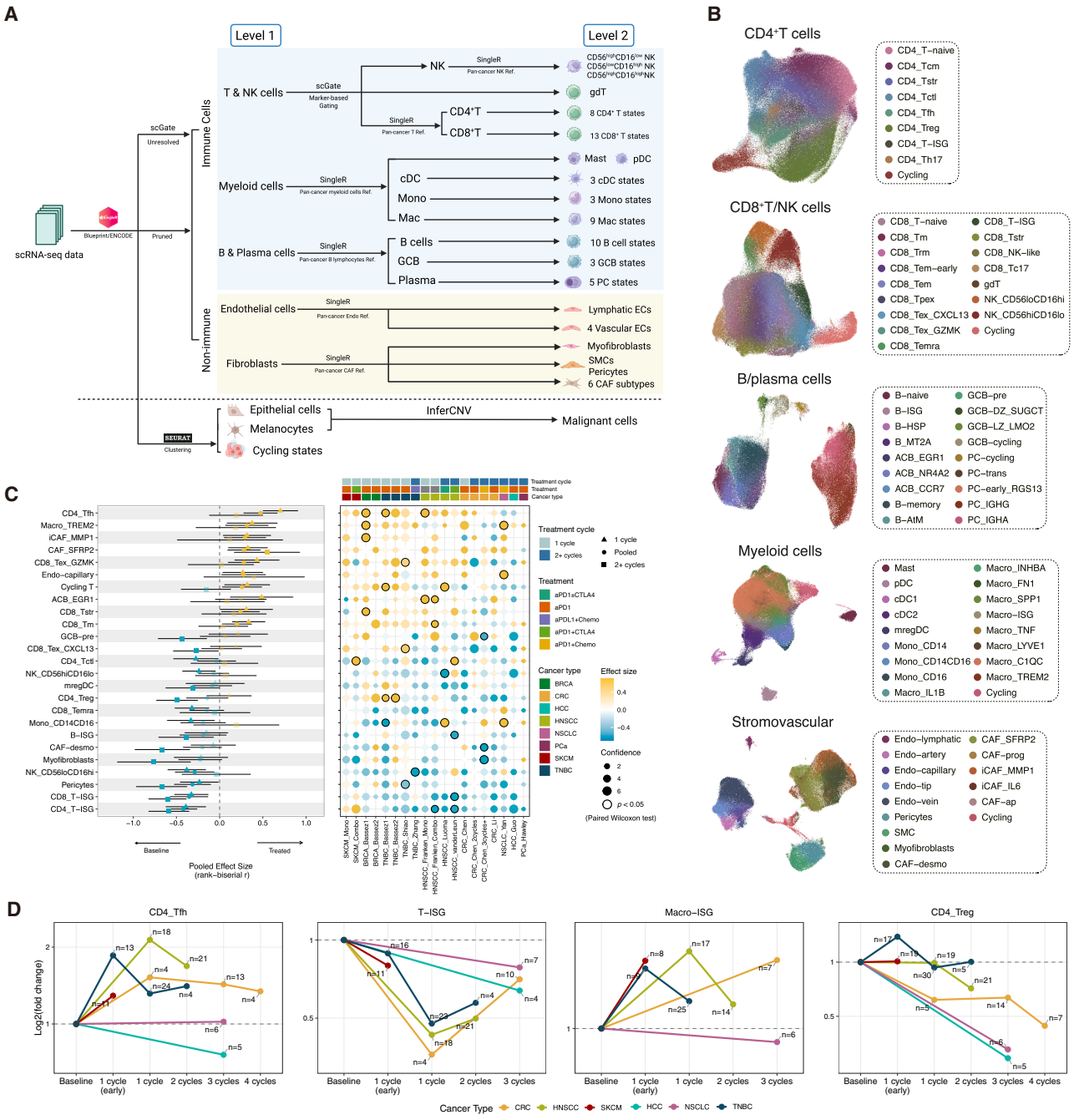


Figure 2. Hierarchical annotation framework and pan-cancer immune landscape

(A) Schematic overview of the two-level reference-guided deep-phenotyping workflow used for hierarchical cell annotation.

(B) Uniform manifold approximation and projection (UMAP) visualization of fine-grained immune and stromal subtypes identified across the integrated pan-cancer atlas.

(C) Meta-analysis of subtype compositional shifts during ICI therapy, showing study-specific estimates (dot plot) and pooled effect sizes (forest plot) for cell subtypes. In the dot plot, colors show the effect size (rank-biserial correlation) of cell types for each cohort, and dot size reflects the confidence of each estimate (inverse of the standard error). The forest plot displays the pooled effect size estimated by a random-effects meta-analysis with restricted maximum likelihood (REML), with 95% confidence intervals indicated by error bars. Statistical testing was performed with paired two-sided Wilcoxon signed-rank test.

(D) Median fold changes for CD4_Tfh, T-ISG, Macro-ISG, and CD4_Treg across treatment time points.

See also Figure S2 and Tables S3 and S4.

Please cite this article in press as: Lin et al., Tumor immune microenvironment remodeling predicts response to checkpoint inhibitor therapy, Cancer Cell (2026), https://doi.org/10.1016/j.ccell.2026.08.007

CellPress

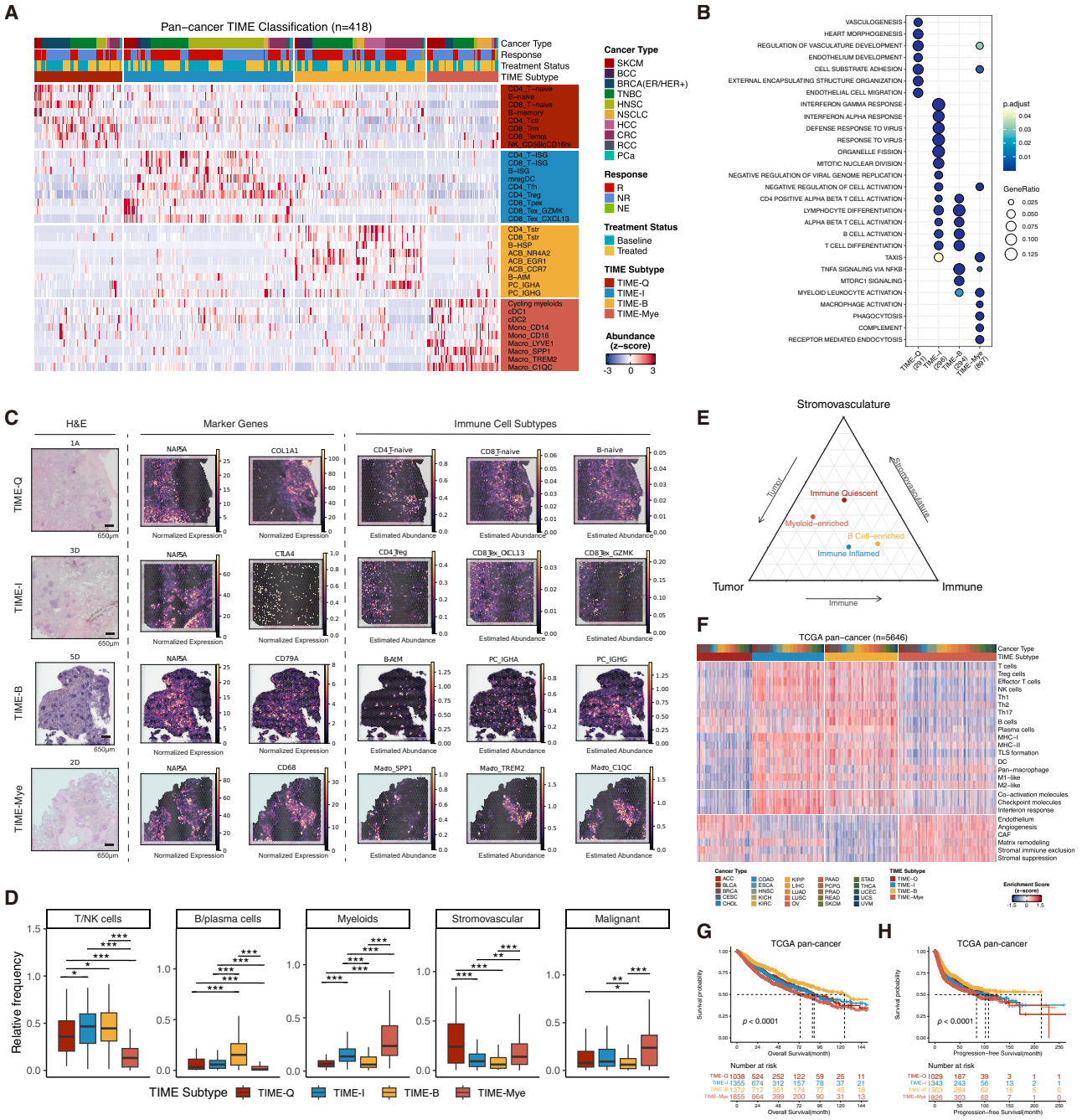


Figure 3. Four distinct TIME subtypes define coordinated immune-stromal organization

(A) Heatmap showing relative cell type abundance of four TIME subtypes, each enriched for distinct immune states. Colors indicate the relative contribution of each cell type; representative cellular modules for each subtype are shown on the right.

(B) Dot plot showing functional pathways enriched for markers of the four TIME subtypes. Statistical significance was determined with a one-tailed Fisher's exact test with Benjamini-Hochberg false discovery rate correction.

(C) Spatial feature plots showing colocalization of representative cell types for TIME subtypes of NSCLC samples, with the color indicating scaled marker gene expression and estimated cellular abundance and the 650 μm scale bars at the bottom right of each H&E slide and colors indicating normalized expression and estimated subtype abundance (percentage).

(D) Boxplots comparing the abundance of broad cell lineages across TIME subtypes. Boxes show the median (central line), the 25%–75% interquartile range (IQR) (box limits), and the ±1.5 IQR (whiskers). Statistical testing by unpaired two-sided Wilcoxon rank-sum test ($p < 0.05$; $^{*}p < 0.01$; $^{**}p < 0.001$; and $^{***}p < 0.0001$). TIME-Q $n = 71$, TIME-I $n = 84$, TIME-B $n = 93$, and TIME-Mye $n = 59$.

(E) Ternary plots showing the distribution of TIME components. The proportions were scaled for visualization.

(legend continued on next page)

Please cite this article in press as: Lin et al., Tumor immune microenvironment remodeling predicts response to checkpoint inhibitor therapy, Cancer Cell (2026), https://doi.org/10.1016/j.ccell.2026.08.007

Macro-ISG increased early and exclusively in responders, indicating that lymphoid and myeloid activations are distinct response-linked processes (Table S4). This finding extends the response-specific interferon signaling kinetics observed in T cells in a preclinical mouse model.[47] Among other immune subtypes, immunosuppressive macrophages (Macro_C1QC and Macro_TREM2) tended to expand preferentially in non-responders, while germinal center B cells increased selectively in responders; at later cycles, CD4_Tfh and CD8_Tex_GZMK accumulation persisted in non-responders but attenuated in responders. Among non-immune subtypes, non-responders showed early expansion of CAF subsets (CAF_SFRP2 and CAF-prog) and endothelial populations (capillary and lymphatic endothelial cells) after a single cycle, whereas responders exhibited pericyte depletion that intensified with extended treatment (Table S4).

Together, these observations delineate the temporal architecture of ICI-associated TIME remodeling: a shared early program of T cell activation and ISG resolution, progressive stromal restructuring, and cancer-type-dependent variation in individual subtype dynamics, with response-stratified analysis revealing a potential link between treatment response and TIME compositional dynamics.

Four distinct TIME subtypes capture coordinated cellular organization

Individual immune-subtype changes typically represented only small fractions of total immune infiltration, making global interpretation difficult. To identify coordinated cellular programs that shape the TIME, we applied non-negative matrix factorization (NMF) to the immune-cell composition profiles from 418 samples, reserving our own melanoma cohort for independent validation (STAR Methods). NMF rank survey metrics and consensus heatmaps identified four as the optimal number of programs (Figures S3A and S3B), which captured major axes of TIME heterogeneity. Each tumor was assigned to a subtype based on its NMF membership scores (Table S5), with clear separation demonstrated by the distinct loading patterns of immune-cell subtypes across the programs (Figure 3A). Because all tumors from the HCC_Guo cohort were mapped to a single subtype, they were excluded from downstream analyses to avoid study-specific bias. NMF classifications showed no significant difference between $CD45^+$-sorted and entire TME samples in HNSCC (with sufficient number of samples), indicating robustness to the sample processing protocol ($p = 0.395$, Fisher's exact test; Table S5).

TIME-I (immune-inflamed) tumors exhibit high infiltration of both adaptive immune cells, including interferon-responsive and *CXCL13*$^+$ T cells, B cells, and plasma cells, alongside inflammatory macrophages (Figure 3A). Functional enrichment confirmed activation of immune-effector and interferon pathways (Figure 3B), although concurrent accumulation of exhausted T cells and regulatory DCs suggested a mixed state characterized by both immune engagement and regulatory suppression mechanisms.[48,49] TIME-B (B cell-enriched) tumors are characterized by abundant activated and atypical memory B cells and plasma cells, accompanied by $CD4^+$ central memory T cells, stressed T cells, and type 17 T cells (Th17 and mucosal-associated invariant T [MAIT]), reflecting active humoral immunity and potential tertiary lymphoid structure (TLS) formation (Figures 3B and S3C). TIME-Mye (myeloid-enriched) tumors are dominated by various myeloid cell populations, including macrophages, monocytes, and DCs, indicative of an immunosuppressive, myeloid-rich environment. TIME-Q (immune quiescent) tumors are defined by early-stage T and B cells and non-exhausted cytotoxic T cells. Additionally, we mapped the fine-grained cell types of each TIME subtype on matched Visium spatial transcriptomic samples to evaluate the spatial distribution pattern (Figure 3C). Notably, in TIME-Q tumors, feature cell types were primarily localized to stromal areas along tumor boundaries, resembling the immune-excluded phenotype previously described in liver cancer (Figure 3C).[50]

Beyond immune composition, the TIME subtypes reflected broader microenvironmental organization. TIME-Q and TIME-Mye displayed higher stromovascular content than TIME-B and TIME-I (Figures 3D and 3E). Inflammatory and antigen-presenting CAF populations were selectively enriched in TIME-B tumors (Figure S3D), supporting the concept of coordinated pro-inflammation immune-stromal interactions within this subtype. Curated TME signature analysis further validated these functional distinctions: TIME-I showed the highest scores for cytotoxicity, co-activation molecules, checkpoint molecules, and interferon response, whereas TIME-B demonstrated elevated Th17 and B/plasma cell signatures (Figures S3E and S3F; Table S6). Cell-cell communication analysis suggested that the interactions among T cells and NK cells in TIME-Q were substantially lower than those in TIME-I and TIME-B (Figure S3G). To assess the robustness of our classification, we scaled the relative proportions of our melanoma validation cohort and recovered the NMF weight for sample assignment (Figure S3H; Table S5). We further extended this validation by processing and annotating a large, independent NSCLC cohort (Figure S3I; Table S5). Visium spatial transcriptomic data of matched samples from our melanoma cohort revealed consistent cellular co-localization (Figure S3J). Collectively, these findings confirm the generalizability of our pan-cancer TIME classification.

To relate our TIME subtypes to the previously established TME frameworks, we projected them onto The Cancer Genome Atlas (TCGA) pan-cancer bulk RNA-seq data (STAR Methods; Figure 3F; Table S7) and compared our subtypes with the conserved subtypes (Figure S4A), pan-cancer immune subtypes (Figure S4B), and carcinoma ecotypes (CEs) (Figure S4C).[9,10,38] The comparison revealed both shared features and key distinctions among systems. TIME-I overlapped most strongly with the "immune-enriched," "IFN-γ-dominant subtype," and CE9, reflecting its high immune lymphocyte infiltration and interferon signaling. TIME-B showed partial similarity to the "immune-enriched" and proinflammatory CE10 clusters, consistent with its

(F) Heatmap of TCGA tumors classified into four distinct TIME subtypes, with colors indicating scaled gene set activities.
(G and H) Kaplan-Meier curves showing overall survival (OS) and progression-free survival (PFS) in TCGA pan-cancer bulk RNA-seq data. Statistical significance was assessed with log rank test.
See also Figures S3 and S4 and Tables S5–S7.

Please cite this article in press as: Lin et al., Tumor immune microenvironment remodeling predicts response to checkpoint inhibitor therapy, Cancer Cell (2026), https://doi.org/10.1016/j.ccell.2026.08.007

activated B cell and plasma cell composition. TIME-Q and TIME-Mye aligned more closely with stromal-enriched and lymphocyte-depleted subtypes such as "fibrotic/depleted" and CE6. TIME-Mye also mapped to "wound healing," "lymphocyte-deficient," and the survival-inferior CE1–CE4 ecotypes, indicating that it captures features from both lymphocyte-desert and myeloid-suppressive microenvironments associated with poor prognosis. Consistent with these biological patterns, TIME-I and TIME-B tumors exhibited the highest tumor mutational burden (TMB), T cell receptor (TCR) richness, and tumor purity (Figure S4D), supporting their classification as immunologically active subtypes.[51] Projecting the single-cell-derived classification onto TCGA bulk transcriptomes also confirmed prognostic relevance: across cancer types, TIME-B showed significantly longer overall and progression-free survival, whereas TIME-Mye was consistently associated with the worst outcomes (Figures 3G and 3H).

To test whether baseline immunotypes also predict outcomes under checkpoint blockade, we transferred the classification to a pan-cancer compendium of 1,988 pre-treatment RNA-seq samples from ICI-treated patients (Table S7).[52] Each sample was assigned with a TIME label (Figure S4E). Baseline response rates were higher for TIME-I (36.9%) and TIME-B (31.1%) than for TIME-Q (22.3%) and TIME-Mye (26.0%) ($p = 0.04$; Figure S4F). In these smaller ICI cohorts, the pre-treatment immunotypes did not significantly separate overall or progression-free survival in the ICI cohorts (Figures S4G and S4H). This divergence indicates that while the subtypes capture intrinsic tumor immunobiology and long-term prognosis, a static baseline label is insufficient once therapy perturbs the microenvironment. These results motivate the shift to longitudinal TIME dynamics as the relevant signal for immunotherapy sensitivity and resistance.

TIME transitions were associated with treatment efficacy

Longitudinal pairing of biopsies across our pan-cancer atlas enabled a systematic analysis of TIME remodeling during ICI therapy. Among 187 tumors, 57.8% ($N = 108$) maintained their baseline subtype through treatment, significantly more than expected by random chance ($p < 0.0001$, exact binomial test; Figure 4A), while the remaining 42.2% ($n = 79$) underwent subtype transitions. These transition rates were consistent across treatment cycle groups ($p = 0.437$, Fisher's exact test) and across cancer types (HNSCC $p = 0.651$; TNBC $p = 0.748$; CRC $p = 1$; Fisher's exact test) (Figure 4B), suggesting treatment-associated TIME reprogramming independent of sampling interval variability.

Treatment outcome was closely tied to these subtype trajectories. Non-responders were enriched for treated TIME-Mye tumors ($p = 0.002$, chi-squared test; Figure 4C), which upregulated immunosuppressive programs, such as M2-like macrophages, phagocytosis inhibition, and matrix remodeling (Figure 4D). This pattern suggests acquisition of a myeloid-dominant, therapy-resistant phenotype. In contrast, responders whose tumors transitioned toward the TIME-I subtype demonstrated a coordinated upregulation of anti-tumor pathways, including enhanced TIME-I signature, checkpoint molecule expression, M1-like macrophage activity, and TLS formation (Figure 4E).

Transition direction differed by outcome. For instance, among patients with baseline TIME-I tumors, responders were significantly more likely to transition toward the TIME-B or TIME-Q subtypes, whereas non-responders showed higher rates of transitions toward the response-unfavorable TIME-Mye subtype ($p = 0.004$, Fisher's exact test; Figure 4F). Within TIME-Q tumors, responders exhibited significantly higher B cell infiltration than non-responders (Figure S4I), suggesting that B cell enrichment is a shared feature of response-associated TIME remodeling.[53] We also found that favorable trajectories varied by cancer type: responders with SKCM and HNSCC preferentially switched to TIME-Q, whereas responsive TNBC tumors were more likely to transition to TIME-B (Figure S4J).

Given that subtype transitions were directly correlated with treatment outcome, we posit that TIME dynamics provide a more informative representation of treatment efficacy. We classified the observed transitions based on clinical outcomes into response-favorable and response-unfavorable categories (Figure 4F). The response-favorable category includes the transitions: TIME-B/I→TIME-B and TIME-Q/Mye→TIME-I (STAR Methods). The response-unfavorable category includes the transitions: maintenance of TIME-Q, TIME-Mye, or TIME-I states, TIME-Q→TIME-Mye, and TIME-B→TIME-Q (STAR Methods). By definition, patients in the response-favorable group exhibited higher objective response rates than those in the response-unfavorable group ($p < 0.001$, chi-squared test, Figure 4G). Across treatment cycle groups, we observed directional consistency in several cancer types (e.g., 57.1% vs. 40.0% in CRC across 1–4 cycles; Figure S4K). TNBC exhibited the strongest discrimination among individual cancer types. To confirm that the early-cycle association is not driven by TNBC alone, we performed a meta-analysis excluding TNBC, which still maintained a homogeneous and significant association during the early treatment cycle (pooled odds ratio [OR] = 4.08, $p = 0.022$, $I^2 = 0\%$; Figure S4L). However, sample sizes at two and more cycles were insufficient to reach individual significance; post-hoc minimum detectable effect (MDE) analysis confirmed that the late-cycle cohorts are statistically underpowered to detect the early-cycle effect (HNSCC: 80% power not achievable with only 19 patients; CRC: MDE OR = 49 vs. early-cycle OR = 5.78). Whether the association is maintained, attenuated, or time point dependent at later cycles remains an open question for future studies with larger multi-time-point cohorts. Despite B cell enrichment being a shared feature of favorable transitions, the transition classification provided more consistent response discrimination than B cell abundance or treated TIME-B status across cancer types (pooled chi-square $p < 0.001$ vs. $p = 0.041$ and $p = 0.034$, respectively; cancer-type-adjusted OR = 4.43 vs. 2.31 and 2.30; Figure S4M; Table S8). Adding transition status to a cancer-type-adjusted B cell-only model significantly improved prediction ($p = 0.00059$, likelihood ratio test), whereas the reverse did not ($p = 0.152$; Figure S4N), confirming that the transition framework captures response-relevant information beyond B cell abundance alone.

To evaluate the reproducibility of these transition patterns in independent datasets, we next applied the classification to bulk RNA-seq cohorts with paired biopsies from 139 ICI-treated patients across multiple cancer types. Using the transition definitions derived from the single-cell atlas, we computed response

Please cite this article in press as: Lin et al., Tumor immune microenvironment remodeling predicts response to checkpoint inhibitor therapy, Cancer Cell (2026), https://doi.org/10.1016/j.ccell.2026.08.007

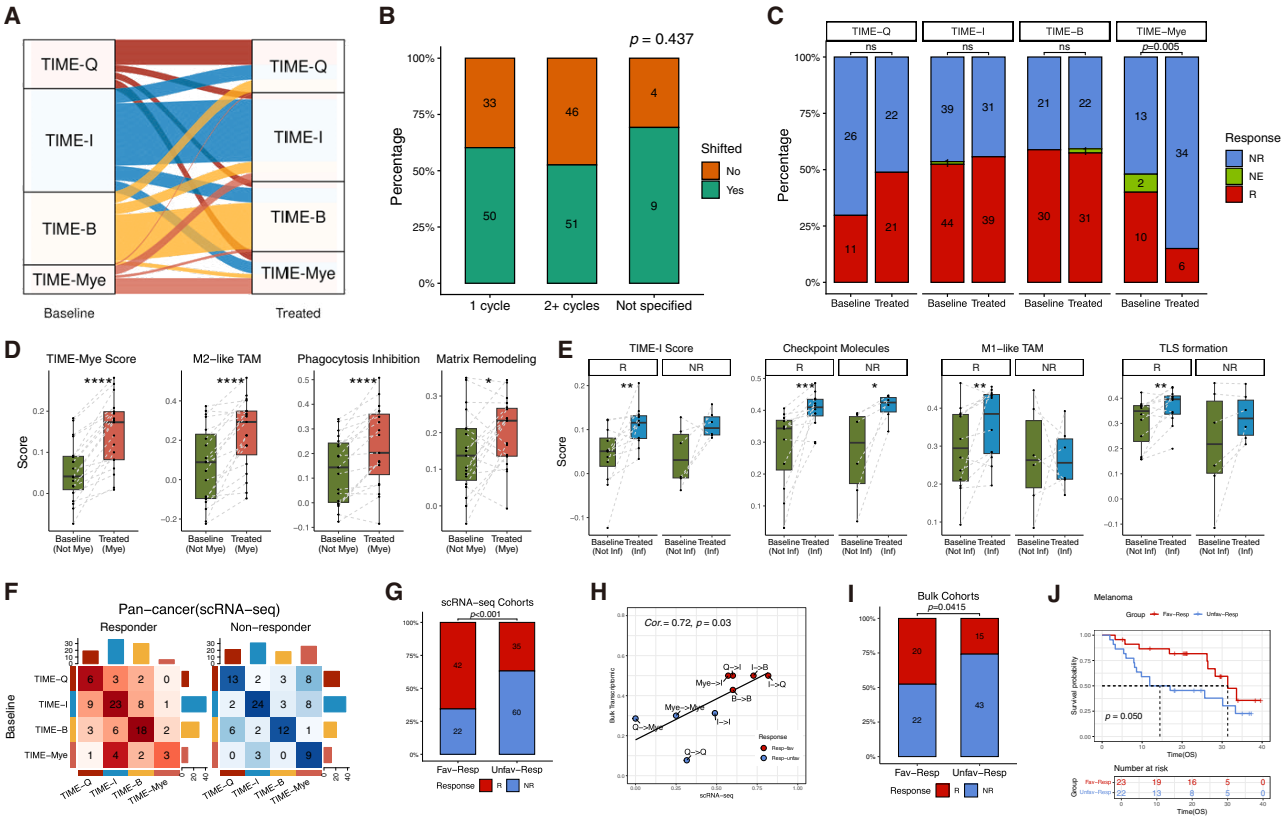


Figure 4. TIME transitions during ICI therapy reflect and predict treatment efficacy

(A) Alluvial diagram showing TIME subtype transitions between the baseline and post-treatment biopsies in ICI-treated tumors.

(B) Bar plot summarizing the proportion of tumors undergoing subtype transitions across different treatment durations; statistical significance was tested with Fisher's exact test.

(C) Distribution of responders and non-responders among baseline and post-treatment TIME subtypes; statistical significance was tested with Fisher's exact test.

(D) Boxplots comparing immune-suppression-related signatures (M2-like macrophages, phagocytosis inhibition, and matrix remodeling) between the baseline and post-treatment samples in tumors that transitioned toward the TIME-Mye subtype ($n = 19$). Statistical testing by paired two-sided Wilcoxon signed-rank test. Boxes show the median (central line), the 25%–75% interquartile range (IQR) (box limits), and the ±1.5 times IQR (whiskers).

(E) Boxplots showing the activation of anti-tumor programs (TIME-I signature, checkpoint-molecule expression, M1-like macrophage polarization, and TLS formation) in tumors transitioning toward the TIME-I subtype, stratified by standardized response (R group $n = 12$; NR $n = 6$). Paired two-sided Wilcoxon signed-rank test. Boxes show the median (central line), the 25%–75% IQR (box limits), and the ±1.5 times IQR (whiskers).

(F) Heatmap displaying the frequency of subtype transitions in responders and non-responders.

(G) Bar plot comparing response rates between the response-favorable and response-unfavorable transition groups defined in the single-cell cohort. Statistical testing was performed with chi-squared test.

(H) Scatterplot showing the correlation of transition-specific response probabilities between single-cell and bulk RNA-seq paired datasets; Spearman's correlation.

(I) Bar plot comparing response rates between the response-favorable and response-unfavorable transitions in paired bulk RNA-seq data. Statistical testing was performed with chi-squared test.

(J) Kaplan-Meier curves showing overall survival for the response-favorable and response-unfavorable transition groups in the melanoma bulk cohort (two-sided log rank test).

$^{*}p < 0.05$, $^{**}p < 0.01$, $^{***}p < 0.001$, $^{****}p < 0.0001$.

See also Figure S4 and Table S8.

probabilities for each transition pattern in the bulk data. These probabilities showed strong concordance between the single-cell and bulk cohorts (r = 0.72, $p = 0.03$, Spearman's correlation test; Figure 4H), confirming that the response-associated dynamics captured by our classification are robust across data modalities. Similarly, patients undergoing response-favorable transitions displayed a higher likelihood of clinical response than those with response-unfavorable transitions ($p = 0.0415$, chi-squared test; Figure 4I). Furthermore, melanoma patients with response-favorable transitions tended to have better overall survival than those with response-unfavorable ones (hazard ratio [HR] = 2.24, 95% confidence interval [CI] = 0.98–5.15, two-sided Cox $p = 0.056$; Figure 4J).

Together, these results demonstrated that TIME transitions detected from paired samples are associated with treatment efficacy and clinical outcome. Monitoring such dynamic remodeling provides a potential surrogate for therapeutic response.

Please cite this article in press as: Lin et al., Tumor immune microenvironment remodeling predicts response to checkpoint inhibitor therapy, Cancer Cell (2026), https://doi.org/10.1016/j.ccell.2026.08.007

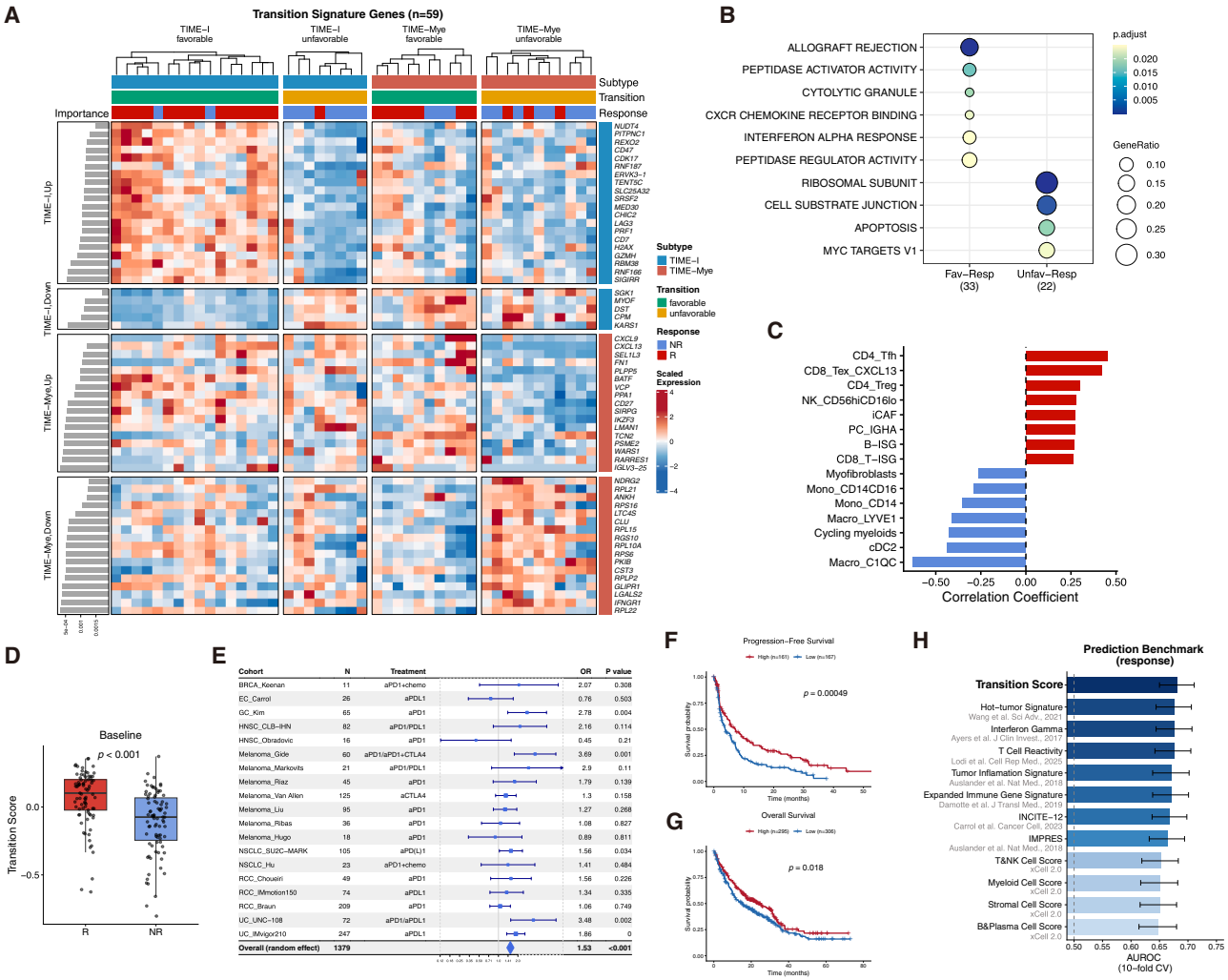


Figure 5. Transition-derived baseline features predict clinical outcome

(A) Heatmap of the genes distinguishing baseline TIME-I and TIME-Mye tumors that transitioned toward TIME-B/Q versus TIME-Mye subtypes during treatment.

(B) Dot plot showing enriched pathways for response-associated transition signature. Statistical significance was determined with a one-tailed Fisher's exact test with Benjamini-Hochberg false discovery rate correction.

(C) Bar plot showing Spearman's correlation coefficients between the transition scores and immune-cell subtype abundance in baseline tumors.

(D) Boxplots comparing the transition scores between responders (n = 81) and non-responders (n = 83) among baseline tumors. Statistical significance was tested with a two-tailed unpaired two-sided Wilcoxon rank-sum test. Boxes show the median (central line), the 25%–75% interquartile range (IQR) (box limits), and the ±1.5 times IQR (whiskers).

(E) The forest plot showing the odds ratios (ORs) for individual cohorts alongside the pooled estimate. The pooled OR was derived from a logistic regression model adjusted for cohort as a covariate. Horizontal error bars indicate 95% confidence intervals, and statistical significance was assessed with the Wald test.

(F and G) Kaplan-Meier analysis of overall survival and progression-free survival stratified by the transition score. Patients were classified into high (Q4, top quartile) and low (Q1, bottom quartile) groups based on within-cohort Z-scored transition signature scores. p values were derived from two-sided log rank test.

(H) Bar plot showing the area under the receiver operating characteristic curve (AUROC) of the transition score, established predictive gene signatures, and immune abundance estimated by xCell 2.0 with 10-fold cross-validation in logistic regression. Error bars represent 95% bootstrap confidence intervals (1,000 iterations).

See also Figure S5 and Table S9.

Response-associated baseline features predict ICI response

Given the close association between TIME transitions and treatment efficacy, we hypothesized that baseline TIME gene expression encodes the intrinsic capacity for favorable or unfavorable transition upon ICI therapy. We focused on TIME-I and TIME-Mye tumors, the two baseline subtypes with the strongest association between transition direction and treatment response. For TIME-I, we compared tumors that transitioned toward TIME-B or TIME-Q (favorable) against those shifting toward TIME-Mye (unfavorable, p = 0.004, Fisher's exact test). For TIME-Mye, we compared tumors that transitioned to other subtypes (favorable) against those that remained myeloid enriched (unfavorable, p = 0.078, Fisher's exact test). Using iterative random forest training

Please cite this article in press as: Lin et al., Tumor immune microenvironment remodeling predicts response to checkpoint inhibitor therapy, Cancer Cell (2026), https://doi.org/10.1016/j.ccell.2026.08.007

on the highly variable genes, we identified 25 discriminative genes from baseline TIME-I tumors and 34 genes from the baseline TIME-Mye tumors (Figures 5A, S5A, and S5B; Table S9).

These two transition patterns uncovered distinct remodeling potential. TIME-I-derived genes defined a "primed" baseline state of cytotoxic effectors (*PRF1* and *GZMH*), and checkpoint receptors (*LAG3*) were upregulated in tumors destined for favorable transitions. TIME-Mye-derived genes instead captured a chemokine and lymphocyte-recruitment program centered on *CXCL9*, *CXCL13*, *BATF*, and *IKZF3*, reflecting preserved capacity for lymphocyte infiltration and TLS formation within an otherwise myeloid-dominated ecotype; unfavorable TIME-Mye tumors were marked by ribosomal protein genes and myeloid immunomodulators (*CST3*, *LGALS2*, and *CLU*). Pathway enrichment confirmed this dichotomy: favorable genes were enriched for allograft rejection, cytolytic granule, and interferon α response programs, while unfavorable genes were enriched for ribosomal biogenesis and MYC targets, a metabolic activation associated with immunosuppressive (M2) macrophage polarization (Figure 5B). Correlation of the transition score with cell type composition across all baseline tumors revealed positive associations with *CXCL13*$^{+}$ T cells and inflammatory CAFs and negative associations with pro-tumor myofibroblasts and immunosuppressive myeloid cells (Figure 5C).

We then combined the two non-overlapping gene sets into a unified 59-gene transition signature (37 up-in-favorable, 22 up-in-unfavorable) and calculated a directional enrichment score to quantify the likelihood of favorable transition for each tumor. In scRNA-seq data, responders had significantly higher transition scores than non-responders ($p < 0.001$, Figure 5D). To validate the transition score as a clinically applicable biomarker, we scored 1,383 baseline samples from 19 independent bulk RNA-seq cohorts of ICI-treated patients spanning multiple cancer types. Adjusted by cohorts, higher transition scores were significantly associated with greater response probability (OR = 1.53, 95% CI: 1.35–1.74, $p < 0.001$; Figure 5E). The directional consistency (16/19) of the signature across heterogeneous cohorts from multiple cancer types suggests its pan-cancer validity; individual-cohort significance ($p < 0.05$) was reached in five cohorts, as expected, given the typical sample sizes of ICI trials. We observed that the transition score did not achieve significance in any of the renal cell carcinoma cohorts, potentially due to its modest TMB and highly dysfunctional immune profile featured by terminally exhausted T cells and suppressive myeloid cells.[54,55] The score also predicted progression-free survival (HR = 0.86, 95% CI: 0.79–0.94, $p < 0.001$; 9 cohorts, n = 657) and overall survival (HR = 0.90, 95% CI: 0.84–0.97, p = 0.008; 14 cohorts, n = 1,204; Figures 5F, 5G, S5C, and S5D). Benchmarking against seven established immunotherapy-response signatures and cell type abundance scores derived from xCell2 estimation, the transition score achieved comparable performance under cohort-adjusted 10-fold cross-validated logistic regression (area under the receiver operating characteristic curve [AUROC] = 0.681, 95% CI: 0.650–0.711; Figure 5H).[52] Notably, the transition score exhibited low correlations with all benchmarked signature scores (r = 0.56–0.72), in contrast to the high intercorrelation among existing predictors (r = 0.70–0.96, Figure S5E). This is consistent with the minimal gene overlap between the transition signature and other signatures (Figure S5F).

Collectively, the 59-gene transition signature, derived from the two transition patterns most strongly linked to response in single-cell data, predicts treatment response and survival across cancer types, capturing non-redundant features relative to existing signatures and providing a scalable measurement of the baseline TIME capacity for favorable transition under checkpoint blockade.

DISCUSSION

Studies following patients with sequential biopsies have been invaluable for revealing the contours of TIME remodeling in cancers such as melanoma, lung, head and neck, breast, liver, and colorectal cancers.[15,20–23,25–28,30,56,57] Yet, these prior analyses have been constrained by sample size. Cohorts of 10–20 paired cases are large for a single-cell study, but they are not powered to resolve modest, clinically relevant effects. The large scale of our pan-cancer atlas, combined with unified cell-type annotation and validation in bulk RNA cohorts, allowed us to identify key TIME subtype transitions associated with treatment efficacy that is more informative than static baseline immunotypes. Furthermore, the transition-derived signature could capture remodeling propensity for patient stratification.

Our reference-guided deep-phenotyping framework aligned cell types with comprehensive pan-cancer reference data across studies and achieved high-resolution annotations while circumventing the over-reliance on integration pipelines that lack consensus benchmarks and reproducibility.[58–61] Across studies, we identified recurrent treatment-associated shifts, including enrichment of CD4_Tfh, *TREM2*$^{+}$ macrophages, and inflammatory cancer-associated fibroblasts, together with the depletion of interferon-responsive T cells. Subgroup analyses by treatment duration and clinical response revealed distinct temporal dynamics—early lymphocyte mobilization followed by progressive stromal restructuring and response-dependent divergence of interferon signaling. Our atlas, therefore, offers a panoramic view of individual cell-type dynamics during ICI therapy.

On the basis of compositional data, we identified four reproducible TIME subtypes that capture coordinated cellular programs. Importantly, each subtype captures coordinated multi-lineage programs beyond single-lineage dominance. Projection onto TCGA data showed that these subtypes are consistent with established classifications but are not redundant to them.[9,10,38] The distinct TIME-B from immune-enriched subtypes exhibited superior prognostic stratification on TCGA primary tumors. In contrast, in a large compendium of pre-treatment biopsies from ICI-treated patients, we found that this baseline classification alone was not directly associated with clinical outcome. Previously, Bagaev et al. reported TIME subtype dynamics on bulk RNA-seq data in melanoma.[9] In our pan-cancer scRNA-seq atlas, we confirmed that a substantial proportion of tumors underwent TIME subtype transitions during the treatment. While the shift rate was constant over time, the specific transitions showed an association with clinical

Please cite this article in press as: Lin et al., Tumor immune microenvironment remodeling predicts response to checkpoint inhibitor therapy, Cancer Cell (2026), https://doi.org/10.1016/j.ccell.2026.08.007

response. Specifically, a shift toward a myeloid-dominant immunosuppressive state correlated with poorer outcomes, while a shift toward a B cell-enriched, immune-activating state was associated with improved response across single-cell and bulk datasets. These patterns place B cell and myeloid dynamics within the broader context of TIME state transitions, reinforcing the interplay between lineage-specific remodeling and coordinated TIME dynamics during therapy.[62,63] We demonstrate that TIME subtype transition could serve as a valuable surrogate biomarker that complements other emerging monitoring strategies, such as circulating T cells and tumor DNA.[64,65]

Combining baseline features from the two most response-associated transition groups, our 59-gene transition signature is found predictive of treatment efficacy. The two constituent gene sets share no overlapping genes and capture complementary biology—cytotoxic and checkpoint programs from inflamed tumors, and chemokine and lymphocyte-recruitment programs from myeloid-enriched tumors. The unified signature predicted clinical outcome across most cohorts and achieved comparable performance in response prediction. Notably, existing ICI response signatures are predominantly derived from T cell activity and are, therefore, highly intercorrelated. By contrast, the transition signature showed minimal gene overlap and substantially lower score correlations with these predictors, indicating that it reflects an alternative biological axis beyond T cell-centric immune activation—the intrinsic capacity for microenvironment remodeling. The signature adds a new dimension to understanding the baseline immune profiles, complementing conventional biomarkers such as PD-L1 expression and TMB.[66,67] The specific mechanisms by which these baseline molecular features impact transition warrant further investigation.

The transition-response association is directionally consistent across every cancer type with paired biopsies in our single-cell atlas, at every sampling interval examined, and across 16 of 19 independent bulk RNA-seq cohorts, establishing it as a pan-cancer property of ICI response. The magnitude of the transition-response association varies across indications, as expected, given heterogeneities in cancer biology, sampling protocols, and treatment regimens. Per-indication calibration, including threshold selection and, where appropriate, indication-specific signatures, are required for clinical decision-making, as it is for every existing ICI response biomarker. The TIME framework provides the underlying organizing principle: a pan-cancer characterization of response-associated remodeling that unifies cancer-type-specific trajectories into a shared, cross-lineage TIME dynamic.

In summary, the field has reached a point where cellular diversity and tissue subtypes are well cataloged; the path to clinical impact requires larger, harmonized, longitudinal resources, and analytical strategies designed for reproducibility and statistical power. Our study provides one such framework and demonstrates the capacity of TIME remodeling to generate reliable, treatment-guiding insights.

Limitations of the study

Several limitations merit attention. As an early investigation to systematically leverage longitudinal scRNA-seq data for pan-cancer analysis of treatment-associated TIME dynamics, this work necessarily contends with constraints inherent to the available data. Despite harmonization, residual batch and sampling biases are possible, including differences in cancer type, biopsy timing, lesion site, prior lines, and concurrent therapies. Moreover, our reference-guided annotation framework prioritizes cross-cancer consistency and may, therefore, underrepresent rare or tissue-resident immune populations whose roles in ICI response are cancer type specific. Response criteria and survival endpoints were not uniform across cohorts, and subgroup analysis of cancer-type-specific dynamics was still limited by sample size. Consequently, while the transition-response association was directionally consistent across cancer types and treatment cycles, whether the transition-response association is genuinely attenuated at later treatment cycles or simply underpowered in the available late-cycle cohorts cannot be resolved with the current data. Furthermore, the absence of untreated longitudinal controls means that the observed changes are treatment associated, rather than definitively treatment induced; to our knowledge, no such datasets exist due to ethical constraints on withholding therapy during serial biopsies. Spatial data remain limited, further constraining mechanistic interpretation. Although validation across single-cell and bulk modalities increases confidence, prospective studies that embed remodeling patterns and decision thresholds are necessary to test clinical utility. Addressing the limitations above requires larger multi-time-point cohorts.

RESOURCE AVAILABILITY

Lead contact

Requests for further information and resources should be directed to and will be addressed by the lead contact, Dvir Aran (dviraran@technion.ac.il).

Materials availability

This study did not generate new unique reagents.

Data and code availability

The raw sequencing data of Essen SKCM cohort have been deposited in the European Genome-phenome Archive under accession number EGAS-50000000459. Processed scRNA-seq and spatial evisium data have been deposited in Zenodo (https://doi.org/10.5281/zenodo.19586163). All scRNA-seq and bulk transcriptomic datasets re-analyzed in this study are accessible from their respective original publications, as detailed in Table S2. The code of the analyses in the study is available at https://github.com/zlin-bioinfo/PanCancer_ICI. Any additional information required to reanalyze the data reported in this paper is available from the lead contact upon request.

ACKNOWLEDGMENTS

This work was funded by the Israel Science Foundation (1543/21) and Azrieli Faculty Fellowship (to D.A.), by Deutsches Konsortium für Translationale Krebsforschung (ED03 to J.C.B.), and Else Kröner-Fresenius-Stiftung (EKFS), University Medicine Essen Medical Scientist Academy (UMESciA) (to N.S.). The graphical abstract and Figures 1A and 2A were created with BioRender.com.

AUTHOR CONTRIBUTIONS

D.A. and J.C.B. conceived the study and supervised the analyses; Z.L. performed all bioinformatics analyses; M.C. and N.S. performed the scRNA-seq; S.U. collected the samples from the patients; D.A. and Z.L. wrote the manuscript with input from J.C.B.

Please cite this article in press as: Lin et al., Tumor immune microenvironment remodeling predicts response to checkpoint inhibitor therapy, Cancer Cell (2026), https://doi.org/10.1016/j.ccell.2026.08.007

DECLARATION OF INTERESTS

S.U. declares research support from Bristol Myers Squibb and Merck Serono; speakers and advisory board honoraria from Bristol Myers Squibb, Merck Sharp & Dohme, Merck Serono, Novartis, and Roche; and travel support from Bristol Myers Squibb, Merck Sharp & Dohme, and Pierre Fabre. J.C.B. is receiving speaker's bureau honoraria from Amgen, Incyte, Merck Serono, Pfizer, and Regeneron and is a paid consultant/advisory board member/DSMB member for Almirall, Boehringer Ingelheim, ICON, Merck Sharp & Dohme, Merck Serono, and Regeneron. His group receives research grants from Merck Serono, IKF, IQVIA, and Alcedis. D.A. is a consultant to Link Cell Therapies.

STAR★METHODS

Detailed methods are provided in the online version of this paper and include the following:

- KEY RESOURCES TABLE
- EXPERIMENTAL MODEL AND STUDY PARTICIPANT DETAILS
  - Study participant details
- METHOD DETAILS
  - Single-cell RNA-seq data generation
  - Spatial transcriptomic data generation
  - Single-cell RNA-seq data curation and standardization
  - Single-cell RNA-seq data preprocessing
  - Hierarchical cell annotation
  - Malignant cell identification
  - Cell type abundance
  - Meta-analysis of inter-cohort compositional analysis
  - Gene set enrichment analysis
  - Differential expression analysis and over-representation enrichment analysis
  - Non-negative matrix factorization (NMF) analysis for identifying tissue-specific cellular programs
  - Assignment of scRNA-seq and bulk transcriptomic data to TIME subtypes
  - Cell-cell interaction analysis
  - Abundance estimation in spatial transcriptomic data
  - Transition classification and comparison with B cell classifiers
  - Development and evaluation of transition-associated signature
- QUANTIFICATION AND STATISTICAL ANALYSIS

SUPPLEMENTAL INFORMATION

Supplemental information can be found online at https://doi.org/10.1016/j.ccell.2026.06.016.

Received: November 24, 2025
Revised: March 11, 2026
Accepted: August 7, 2026

REFERENCES

1. Robert, C., Ribas, A., Wolchok, J.D., Hodi, F.S., Hamid, O., Kefford, R., Weber, J.S., Joshua, A.M., Hwu, W.-J., Gangadhar, T.C., et al. (2014). Anti-programmed-death-receptor-1 treatment with pembrolizumab in ipilimumab-refractory advanced melanoma: a randomised dose-comparison cohort of a phase 1 trial. Lancet *384*, 1109–1117. https://doi.org/10.1016/S0140-6736(14)60958-2.
2. Motzer, R.J., Rini, B.I., McDermott, D.F., Redman, B.G., Kuzel, T.M., Harrison, M.R., Vaishampayan, U.N., Drabkin, H.A., George, S., Logan, T.F., et al. (2015). Nivolumab for Metastatic Renal Cell Carcinoma: Results of a Randomized Phase II Trial. J. Clin. Oncol. *33*, 1430–1437. https://doi.org/10.1200/jco.2014.59.0703.
3. Ferris, R.L., Blumenschein, G., Jr., Fayette, J., Guigay, J., Colevas, A.D., Licitra, L., Harrington, K., Kasper, S., Vokes, E.E., Even, C., et al. (2016). Nivolumab for Recurrent Squamous-Cell Carcinoma of the Head and Neck. N. Engl. J. Med. *375*, 1856–1867. https://doi.org/10.1056/NEJMoa1602252.
4. Ansell, S.M., Lesokhin, A.M., Borrello, I., Halwani, A., Scott, E.C., Gutierrez, M., Schuster, S.J., Millenson, M.M., Cattry, D., Freeman, G.J., et al. (2015). PD-1 blockade with nivolumab in relapsed or refractory Hodgkin's lymphoma. N. Engl. J. Med. *372*, 311–319. https://doi.org/10.1056/NEJMoa1411087.
5. Aran, D. (2023). Single-Cell RNA Sequencing for Studying Human Cancers. Annu. Rev. Biomed. Data Sci. *6*, 1–22. https://doi.org/10.1146/annurev-biodatasci-020722-091857.
6. Aliazis, K., Christofides, A., Shah, R., Yeo, Y.Y., Jiang, S., Charest, A., and Boussiotis, V.A. (2025). The tumor microenvironment's role in the response to immune checkpoint blockade. Nat. Cancer *6*, 924–937. https://doi.org/10.1038/s43018-025-00986-3.
7. Wu, B., Zhang, B., Li, B., Wu, H., and Jiang, M. (2024). Cold and hot tumors: from molecular mechanisms to targeted therapy. Signal Transduct. Targeted Ther. *9*, 274. https://doi.org/10.1038/s41392-024-01979-x.
8. Galon, J., and Bruni, D. (2019). Approaches to treat immune hot, altered and cold tumours with combination immunotherapies. Nat. Rev. Drug Discov. *18*, 197–218. https://doi.org/10.1038/s41573-018-0007-y.
9. Bagaev, A., Kotlov, N., Nomie, K., Svekolkin, V., Gafurov, A., Isaeva, O., Osokin, N., Kozlov, I., Frenkel, F., Gancharova, O., et al. (2021). Conserved pan-cancer microenvironment subtypes predict response to immunotherapy. Cancer Cell *39*, 845–865.e7. https://doi.org/10.1016/j.ccell.2021.04.014.
10. Thorsson, V., Gibbs, D.L., Brown, S.D., Wolf, D., Bortone, D.S., Ou Yang, T.H., Porta-Pardo, E., Gao, G.F., Plaisier, C.L., Eddy, J.A., et al. (2018). The Immune Landscape of Cancer. Immunity *48*, 812–830.e14. https://doi.org/10.1016/j.immuni.2018.03.023.
11. Liu, B., Zhang, Y., Wang, D., Hu, X., and Zhang, Z. (2022). Single-cell meta-analyses reveal responses of tumor-reactive CXCL13+ T cells to immune-checkpoint blockade. Nat. Cancer *3*, 1123–1136. https://doi.org/10.1038/s43018-022-00433-7.
12. Williams, H.L., Frei, A.L., Koessler, T., Berger, M.D., Dawson, H., Michielin, O., and Zlobec, I. (2024). The current landscape of spatial biomarkers for prediction of response to immune checkpoint inhibition. npj Precis. Oncol. *8*, 178. https://doi.org/10.1038/s41698-024-00671-1.
13. Lodi, F., Vanmassenhove, S., Chen, D., Boeckx, B., Ferreira Maciel, L., Peeters, F., Donders, E., Song, H., Harbers, L., Poźniak, J., et al. (2025). Decoding tumor heterogeneity: A spatially informed pan-cancer analysis of the tumor microenvironment. Cell Rep. Med. *6*, 102416. https://doi.org/10.1016/j.xcrm.2025.102416.
14. Naidus, E., Bouquet, J., Oh, D.Y., Looney, T.J., Yang, H., Fong, L., Standifer, N.E., and Zhang, L. (2021). Early changes in the circulating T cells are associated with clinical outcomes after PD-L1 blockade by durvalumab in advanced NSCLC patients. Cancer Immunol. Immunother. *70*, 2095–2102. https://doi.org/10.1007/s00262-020-02833-z.
15. Yost, K.E., Satpathy, A.T., Wells, D.K., Qi, Y., Wang, C., Kageyama, R., McNamara, K.L., Granja, J.M., Sarin, K.Y., Brown, R.A., et al. (2019). Clonal replacement of tumor-specific T cells following PD-1 blockade. Nat. Med. *25*, 1251–1259. https://doi.org/10.1038/s41591-019-0522-3.
16. Riaz, N., Havel, J.J., Makarov, V., Desrichard, A., Urba, W.J., Sims, J.S., Hodi, F.S., Martín-Algarra, S., Mandal, R., Sharfman, W.H., et al. (2017). Tumor and Microenvironment Evolution during Immunotherapy with Nivolumab. Cell *171*, 934–949.e16. https://doi.org/10.1016/j.cell.2017.09.028.
17. Jerby-Arnon, L., Shah, P., Cuoco, M.S., Rodman, C., Su, M.J., Melms, J.C., Leeson, R., Kanodia, A., Mei, S., Lin, J.R., et al. (2018). A Cancer Cell Program Promotes T Cell Exclusion and Resistance to Checkpoint Blockade. Cell *175*, 984–997.e24. https://doi.org/10.1016/j.cell.2018.09.006.

Please cite this article in press as: Lin et al., Tumor immune microenvironment remodeling predicts response to checkpoint inhibitor therapy, Cancer Cell (2026), https://doi.org/10.1016/j.ccell.2026.08.007

18. Zemek, R.M., Anagnostou, V., Pires da Silva, I., Long, G.V., and Lesterhuis, W.J. (2024). Exploiting temporal aspects of cancer immunotherapy. Nat. Rev. Cancer *24*, 480–497. https://doi.org/10.1038/s41568-024-00699-2.

19. Gide, T.N., Quek, C., Menzies, A.M., Tasker, A.T., Shang, P., Holst, J., Madore, J., Lim, S.Y., Velickovic, R., Wongchenko, M., et al. (2019). Distinct Immune Cell Populations Define Response to Anti-PD-1 Monotherapy and Anti-PD-1/Anti-CTLA-4 Combined Therapy. Cancer Cell *35*, 238–255.e6. https://doi.org/10.1016/j.ccell.2019.01.003.

20. Bassez, A., Vos, H., Van Dyck, L., Floris, G., Arijs, I., Desmedt, C., Boeckx, B., Vanden Bempt, M., Nevelsteen, I., Lambein, K., et al. (2021). A single-cell map of intratumoral changes during anti-PD1 treatment of patients with breast cancer. Nat. Med. *27*, 820–832. https://doi.org/10.1038/s41591-021-01323-8.

21. Zhang, Y., Chen, H., Mo, H., Hu, X., Gao, R., Zhao, Y., Liu, B., Niu, L., Sun, X., Yu, X., et al. (2021). Single-cell analyses reveal key immune cell subsets associated with response to PD-L1 blockade in triple-negative breast cancer. Cancer Cell *39*, 1578–1593.e8. https://doi.org/10.1016/j.ccell.2021.09.010.

22. Luoma, A.M., Suo, S., Wang, Y., Gunasti, L., Porter, C.B.M., Nabilsi, N., Tadros, J., Ferretti, A.P., Liao, S., Gurer, C., et al. (2022). Tissue-resident memory and circulating T cells are early responders to pre-surgical cancer immunotherapy. Cell *185*, 2918–2935.e29. https://doi.org/10.1016/j.cell.2022.06.018.

23. Li, J., Wu, C., Hu, H., Qin, G., Wu, X., Bai, F., Zhang, J., Cai, Y., Huang, Y., Wang, C., et al. (2023). Remodeling of the immune and stromal cell compartment by PD-1 blockade in mismatch repair-deficient colorectal cancer. Cancer Cell *41*, 1152–1169.e7. https://doi.org/10.1016/j.ccell.2023.04.011.

24. Hawley, J.E., Obradovic, A.Z., Dallos, M.C., Lim, E.A., Runcie, K., Ager, C.R., McKiernan, J., Anderson, C.B., Decastro, G.J., Weintraub, J., et al. (2023). Anti-PD-1 immunotherapy with androgen deprivation therapy induces robust immune infiltration in metastatic castration-sensitive prostate cancer. Cancer Cell *41*, 1972–1988.e5. https://doi.org/10.1016/j.ccell.2023.10.006.

25. van der Leun, A.M., Traets, J.J.H., Vos, J.L., Elbers, J.B.W., Patiwael, S., Qiao, X., Machuca-Ostos, M., Thommen, D.S., Haanen, J.B.A.G., Schumacher, T.N.M., and Zuur, C.L. (2023). Dual Immune Checkpoint Blockade Induces Analogous Alterations in the Dysfunctional CD8+ T-cell and Activated Treg Compartment. Cancer Discov. *13*, 2212–2227. https://doi.org/10.1158/2159-8290.CD-22-0851.

26. Franken, A., Bila, M., Mechels, A., Kint, S., Van Dessel, J., Pomella, V., Vanuytven, S., Philips, G., Bricard, O., Xiong, J., et al. (2024). CD4+ T cell activation distinguishes response to anti-PD-L1+anti-CTLA4 therapy from anti-PD-L1 monotherapy. Immunity *57*, 541–558.e7. https://doi.org/10.1016/j.immuni.2024.02.007.

27. Shiao, S.L., Gouin, K.H., III, Ing, N., Ho, A., Basho, R., Shah, A., Mebane, R.H., Zitser, D., Martinez, A., Mevises, N.Y., et al. (2024). Single-cell and spatial profiling identify three response trajectories to pembrolizumab and radiation therapy in triple negative breast cancer. Cancer Cell *42*, 70–84.e8. https://doi.org/10.1016/j.ccell.2023.12.012.

28. Chen, Y., Wang, D., Li, Y., Qi, L., Si, W., Bo, Y., Chen, X., Ye, Z., Fan, H., Liu, B., et al. (2024). Spatiotemporal single-cell analysis decodes cellular dynamics underlying different responses to immunotherapy in colorectal cancer. Cancer Cell *42*, 1268–1285.e7. https://doi.org/10.1016/j.ccell.2024.06.009.

29. Yan, Y., Sun, D., Hu, J., Chen, Y., Sun, L., Yu, H., Xiong, Y., Huang, Z., Xia, H., Zhu, X., et al. (2024). Multi-omic profiling highlights factors associated with resistance to immuno-chemotherapy in non-small-cell lung cancer. Nat. Genet. *57*, 126–139. https://doi.org/10.1038/s41588-024-01998-y.

30. Guo, X., Nie, H., Zhang, W., Li, J., Ge, J., Xie, B., Hu, W., Zhu, Y., Zhong, N., Zhang, X., et al. (2025). Contrasting cytotoxic and regulatory T cell responses underlying distinct clinical outcomes to anti-PD-1 plus lenvatinib therapy in cancer. Cancer Cell *43*, 248–268.e9. https://doi.org/10.1016/j.ccell.2025.01.001.

31. Zheng, L., Qin, S., Si, W., Wang, A., Xing, B., Gao, R., Ren, X., Wang, L., Wu, X., Zhang, J., et al. (2021). Pan-cancer single-cell landscape of tumor-infiltrating T cells. Science *374*, abe6474. https://doi.org/10.1126/science.abe6474.

32. Qian, J., Olbrecht, S., Boeckx, B., Vos, H., Laoui, D., Etlioglu, E., Wauters, E., Pomella, V., Verbandt, S., Busschaert, P., et al. (2020). A pan-cancer blueprint of the heterogeneous tumor microenvironment revealed by single-cell profiling. Cell Res. *30*, 745–762. https://doi.org/10.1038/s41422-020-0355-0.

33. Cheng, S., Li, Z., Gao, R., Xing, B., Gao, Y., Yang, Y., Qin, S., Zhang, L., Ouyang, H., Du, P., et al. (2021). A pan-cancer single-cell transcriptional atlas of tumor infiltrating myeloid cells. Cell *184*, 792–809.e23. https://doi.org/10.1016/j.cell.2021.01.010.

34. Luo, H., Xia, X., Huang, L.-B., An, H., Cao, M., Kim, G.D., Chen, H.-N., Zhang, W.-H., Shu, Y., Kong, X., et al. (2022). Pan-cancer single-cell analysis reveals the heterogeneity and plasticity of cancer-associated fibroblasts in the tumor microenvironment. Nat. Commun. *13*, 6619. https://doi.org/10.1038/s41467-022-34395-2.

35. Tang, F., Li, J., Qi, L., Liu, D., Bo, Y., Qin, S., Miao, Y., Yu, K., Hou, W., Li, J., et al. (2023). A pan-cancer single-cell panorama of human natural killer cells. Cell *186*, 4235–4251.e20. https://doi.org/10.1016/j.cell.2023.07.034.

36. Kang, J., Lee, J.H., Cha, H., An, J., Kwon, J., Lee, S., Kim, S., Baykan, M.Y., Kim, S.Y., An, D., et al. (2024). Systematic dissection of tumor-normal single-cell ecosystems across a thousand tumors of 30 cancer types. Nat. Commun. *15*, 4067. https://doi.org/10.1038/s41467-024-48310-4.

37. Ma, J., Wu, Y., Ma, L., Yang, X., Zhang, T., Song, G., Li, T., Gao, K., Shen, X., Lin, J., et al. (2024). A blueprint for tumor-infiltrating B cells across human cancers. Science *384*, eadj4857. https://doi.org/10.1126/science.adj4857.

38. Luca, B.A., Steen, C.B., Matusiak, M., Azizi, A., Varma, S., Zhu, C., Przybyl, J., Espín-Pérez, A., Diehn, M., Alizadeh, A.A., et al. (2021). Atlas of clinically distinct cell states and ecosystems across human solid tumors. Cell *184*, 5482–5496.e28. https://doi.org/10.1016/j.cell.2021.09.014.

39. Aran, D., Looney, A.P., Liu, L., Wu, E., Fong, V., Hsu, A., Chak, S., Naikawadi, R.P., Wolters, P.J., Abate, A.R., et al. (2019). Reference-based analysis of lung single-cell sequencing reveals a transitional profibrotic macrophage. Nat. Immunol. *20*, 163–172. https://doi.org/10.1038/s41590-018-0276-y.

40. Andreatta, M., Berenstein, A.J., and Carmona, S.J. (2022). scGate: marker-based purification of cell types from heterogeneous single-cell RNA-seq datasets. Bioinformatics *38*, 2642–2644. https://doi.org/10.1093/bioinformatics/btac141.

41. Büttner, M., Ostner, J., Müller, C.L., Theis, F.J., and Schubert, B. (2021). scCODA is a Bayesian model for compositional single-cell data analysis. Nat. Commun. *12*, 6876. https://doi.org/10.1038/s41467-021-27150-6.

42. Barry, K.C., Hsu, J., Broz, M.L., Cueto, F.J., Binnewies, M., Combes, A.J., Nelson, A.E., Loo, K., Kumar, R., Rosenblum, M.D., et al. (2018). A natural killer–dendritic cell axis defines checkpoint therapy–responsive tumor microenvironments. Nat. Med. *24*, 1178–1191. https://doi.org/10.1038/s41591-018-0085-8.

43. Chu, Y., Dai, E., Li, Y., Han, G., Pei, G., Ingram, D.R., Thakkar, K., Qin, J.J., Dang, M., Le, X., et al. (2023). Pan-cancer T cell atlas links a cellular stress response state to immunotherapy resistance. Nat. Med. *29*, 1550–1562. https://doi.org/10.1038/s41591-023-02371-y.

44. Yang, Y., Chen, X., Pan, J., Ning, H., Zhang, Y., Bo, Y., Ren, X., Li, J., Qin, S., Wang, D., et al. (2024). Pan-cancer single-cell dissection reveals phenotypically distinct B cell subtypes. Cell *187*, 4790–4811.e22. https://doi.org/10.1016/j.cell.2024.06.038.

45. Pan, X., Li, X., Dong, L., Liu, T., Zhang, M., Zhang, L., Zhang, X., Huang, L., Shi, W., Sun, H., et al. (2024). Tumour vasculature at single-cell resolution. Nature *632*, 429–436. https://doi.org/10.1038/s41586-024-07698-1.

46. Gao, Y., Li, J., Cheng, W., Diao, T., Liu, H., Bo, Y., Liu, C., Zhou, W., Chen, M., Zhang, Y., et al. (2024). Cross-tissue human fibroblast atlas reveals myofibroblast subtypes with distinct roles in immune modulation.

Please cite this article in press as: Lin et al., Tumor immune microenvironment remodeling predicts response to checkpoint inhibitor therapy, Cancer Cell (2026), https://doi.org/10.1016/j.ccell.2026.08.007

Cancer Cell *42*, 1764–1783.e10. https://doi.org/10.1016/j.ccell.2024.08.020.

47. Zemek, R.M., Chin, W.L., Fear, V.S., Wylie, B., Casey, T.H., Forbes, C., Tilsed, C.M., Boon, L., Guo, B.B., Bosco, A., et al. (2022). Temporally restricted activation of IFNβ signaling underlies response to immune checkpoint therapy in mice. Nat. Commun. *13*, 4895. https://doi.org/10.1038/s41467-022-32567-8.
48. Pelka, K., Hofree, M., Chen, J.H., Sarkizova, S., Pirl, J.D., Jorgji, V., Bejnood, A., Dionne, D., Ge, W.H., Xu, K.H., et al. (2021). Spatially organized multicellular immune hubs in human colorectal cancer. Cell *184*, 4734–4752.e20. https://doi.org/10.1016/j.cell.2021.08.003.
49. Combes, A.J., Samad, B., Tsui, J., Chew, N.W., Yan, P., Reeder, G.C., Kushnoor, D., Shen, A., Davidson, B., Barczak, A.J., et al. (2022). Discovering dominant tumor immune archetypes in a pan-cancer census. Cell *185*, 184–203.e19. https://doi.org/10.1016/j.cell.2021.12.004.
50. Xue, R., Zhang, Q., Cao, Q., Kong, R., Xiang, X., Liu, H., Feng, M., Wang, F., Cheng, J., Li, Z., et al. (2022). Liver tumour immune microenvironment subtypes and neutrophil heterogeneity. Nature *612*, 141–147. https://doi.org/10.1038/s41586-022-05400-x.
51. Niknafs, N., Balan, A., Cherry, C., Hummelink, K., Monkhorst, K., Shao, X.M., Belcaid, Z., Marrone, K.A., Murray, J., Smith, K.N., et al. (2023). Persistent mutation burden drives sustained anti-tumor immune responses. Nat. Med. *29*, 440–449. https://doi.org/10.1038/s41591-022-02163-w.
52. Angel, A., Naom, L., Nabet-Levy, S., and Aran, D. (2025). xCell 2.0: robust algorithm for cell type proportion estimation predicts response to immune checkpoint blockade. Genome Biol. *26*, 335. https://doi.org/10.1186/s13059-025-03784-3.
53. Patil, N.S., Nabet, B.Y., Müller, S., Koeppen, H., Zou, W., Giltnane, J., Au-Yeung, A., Srivats, S., Cheng, J.H., Takahashi, C., et al. (2022). Intratumoral plasma cells predict outcomes to PD-L1 blockade in non-small cell lung cancer. Cancer Cell *40*, 289–300.e4. https://doi.org/10.1016/j.ccell.2022.02.002.
54. Alexandrov, L.B., Nik-Zainal, S., Wedge, D.C., Aparicio, S.A.J.R., Behjati, S., Biankin, A.V., Bignell, G.R., Bolli, N., Borg, A., Børresen-Dale, A.-L., et al. (2013). Signatures of mutational processes in human cancer. Nature *500*, 415–421. https://doi.org/10.1038/nature12477.
55. Braun, D.A., Street, K., Burke, K.P., Cookmeyer, D.L., Denize, T., Pedersen, C.B., Gohil, S.H., Schindler, N., Pomerance, L., Hirsch, L., et al. (2021). Progressive immune dysfunction with advancing disease stage in renal cell carcinoma. Cancer Cell *39*, 632–648.e8. https://doi.org/10.1016/j.ccell.2021.02.013.
56. Pozniak, J., Pedri, D., Landeloos, E., Van Herck, Y., Antoranz, A., Vanwynsberghe, L., Nowosad, A., Roda, N., Makhzami, S., Bervoets, G., et al. (2024). A TCF4-dependent gene regulatory network confers resistance to immunotherapy in melanoma. Cell *187*, 166–183.e25. https://doi.org/10.1016/j.cell.2023.11.037.
57. Ma, L., Wang, L., Khatib, S.A., Chang, C.W., Heinrich, S., Dominguez, D.A., Forgues, M., Candia, J., Hernandez, M.O., Kelly, M., et al. (2021). Single-cell atlas of tumor cell evolution in response to therapy in hepatocellular carcinoma and intrahepatic cholangiocarcinoma. J. Hepatol. *75*, 1397–1408. https://doi.org/10.1016/j.jhep.2021.06.028.
58. Rautenstrauch, P., and Ohler, U. (2025). Shortcomings of silhouette in single-cell integration benchmarking. Nat. Biotechnol. *44*, 954–958. https://doi.org/10.1038/s41587-025-02743-4.
59. Wang, H., Leskovec, J., and Regev, A. (2025). Limitations of cell embedding metrics assessed using drifting islands. Nat. Biotechnol. *44*, 574–577. https://doi.org/10.1038/s41587-025-02702-z.
60. Luecken, M.D., Büttner, M., Chaichoompu, K., Danese, A., Interlandi, M., Mueller, M.F., Strobl, D.C., Zappia, L., Dugas, M., Colomé-Tatché, M., and Theis, F.J. (2022). Benchmarking atlas-level data integration in single-cell genomics. Nat. Methods *19*, 41–50. https://doi.org/10.1038/s41592-021-01336-8.
61. Tirosh, I. (2026). Pitfalls in analysis and interpretation of single-cell RNA-seq data in cancer. Neurooncol. Adv. *8*, i57–i60. https://doi.org/10.1093/noajnl/vdaf047.
62. Flippot, R., Teixeira, M., Rey-Cardenas, M., Carril-Ajuria, L., Rainho, L., Naoun, N., Jouniaux, J.M., Boselli, L., Naigeon, M., Danlos, F.X., et al. (2024). B cells and the coordination of immune checkpoint inhibitor response in patients with solid tumors. J. Immunother. Cancer *12*, e008636. https://doi.org/10.1136/jitc-2023-008636.
63. Nakamura, K., and Smyth, M.J. (2020). Myeloid immunosuppression and immune checkpoints in the tumor microenvironment. Cell. Mol. Immunol. *17*, 1–12. https://doi.org/10.1038/s41423-019-0306-1.
64. Abbosh, C., Hodgson, D., Doherty, G.J., Gale, D., Black, J.R.M., Horn, L., Reis-Filho, J.S., and Swanton, C. (2024). Implementing circulating tumor DNA as a prognostic biomarker in resectable non-small cell lung cancer. Trends Cancer *10*, 643–654. https://doi.org/10.1016/j.trecan.2024.04.004.
65. Hwang, M., Canzoniero, J.V., Rosner, S., Zhang, G., White, J.R., Belcaid, Z., Cherry, C., Balan, A., Pereira, G., Curry, A., et al. (2022). Peripheral blood immune cell dynamics reflect antitumor immune responses and predict clinical response to immunotherapy. J. Immunother. Cancer *10*, e004688. https://doi.org/10.1136/jitc-2022-004688.
66. Luchini, C., Bibeau, F., Ligtenberg, M.J.L., Singh, N., Nottegar, A., Bosse, T., Miller, R., Riaz, N., Douillard, J.Y., Andre, F., and Scarpa, A. (2019). ESMO recommendations on microsatellite instability testing for immunotherapy in cancer, and its relationship with PD-1/PD-L1 expression and tumour mutational burden: a systematic review-based approach. Ann. Oncol. *30*, 1232–1243. https://doi.org/10.1093/annonc/mdz116.
67. Rizvi, H., Sanchez-Vega, F., La, K., Chatila, W., Jonsson, P., Halpenny, D., Plodkowski, A., Long, N., Sauter, J.L., Rekhtman, N., et al. (2018). Molecular Determinants of Response to Anti-Programmed Cell Death (PD)-1 and Anti-Programmed Death-Ligand 1 (PD-L1) Blockade in Patients With Non-Small-Cell Lung Cancer Profiled With Targeted Next-Generation Sequencing. J. Clin. Oncol. *36*, 633–641. https://doi.org/10.1200/jco.2017.75.3384.
68. Hao, Y., Stuart, T., Kowalski, M.H., Choudhary, S., Hoffman, P., Hartman, A., Srivastava, A., Molla, G., Madad, S., Fernandez-Granda, C., and Satija, R. (2023). Dictionary learning for integrative, multimodal and scalable single-cell analysis. Nat. Biotechnol. *42*, 293–304. https://doi.org/10.1038/s41587-023-01767-y.
69. Germain, P.-L., Lun, A., Garcia Meixide, C., Macnair, W., and Robinson, M.D. (2022). Doublet identification in single-cell sequencing data using scDblFinder. F1000Res. *10*, 979. https://doi.org/10.12688/f1000research.73600.2.
70. McGinnis, C.S., Murrow, L.M., and Gartner, Z.J. (2019). DoubletFinder: Doublet Detection in Single-Cell RNA Sequencing Data Using Artificial Nearest Neighbors. Cell Syst. *8*, 329–337.e4. https://doi.org/10.1016/j.cels.2019.03.003.
71. Korsunsky, I., Millard, N., Fan, J., Slowikowski, K., Zhang, F., Wei, K., Baglaenko, Y., Brenner, M., Loh, P.R., and Raychaudhuri, S. (2019). Fast, sensitive and accurate integration of single-cell data with Harmony. Nat. Methods *16*, 1289–1296. https://doi.org/10.1038/s41592-019-0619-0.
72. Tickle T, Georgescu C, Brown M, Haas B (2019). inferCNV of the Trinity CTAT Project. https://github.com/broadinstitute/inferCNV
73. Mangiafico, S. (2024). rcompanion: Functions to Support Extension Education Program Evaluation. CRAN. https://doi.org/10.32614/CRAN.package.rcompanion.
74. Viechtbauer, W. (2010). Conducting Meta-Analyses in R with the metafor Package. J. Stat. Software *36*, 1–48. https://doi.org/10.18637/jss.v036.i03.
75. Hänzelmann, S., Castelo, R., and Guinney, J. (2013). GSVA: gene set variation analysis for microarray and RNA-Seq data. BMC Bioinf. *14*, 7. https://doi.org/10.1186/1471-2105-14-7.
76. Wu, T., Hu, E., Xu, S., Chen, M., Guo, P., Dai, Z., Feng, T., Zhou, L., Tang, W., Zhan, L., et al. (2021). clusterProfiler 4.0: A universal enrichment tool for interpreting omics data. Innovation *2*, 100141. https://doi.org/10.1016/j.xinn.2021.100141.
77. Kleshchevnikov, V., Shmatko, A., Dann, E., Aivazidis, A., King, H.W., Li, T., Elmentaite, R., Lomakin, A., Kedlian, V., Gayoso, A., et al. (2022).

Please cite this article in press as: Lin et al., Tumor immune microenvironment remodeling predicts response to checkpoint inhibitor therapy, Cancer Cell (2026), https://doi.org/10.1016/j.ccell.2026.08.007

Cell2location maps fine-grained cell types in spatial transcriptomics. Nat. Biotechnol. *40*, 661–671. https://doi.org/10.1038/s41587-021-01139-4.

78. Jin, S., Plikus, M.V., and Nie, Q. (2025). CellChat for systematic analysis of cell–cell communication from single-cell transcriptomics. Nat. Protoc. *20*, 180–219. https://doi.org/10.1038/s41596-024-01045-4.

79. Wolf, F.A., Angerer, P., and Theis, F.J. (2018). SCANPY: large-scale single-cell gene expression data analysis. Genome Biol. *19*, 15. https://doi.org/10.1186/s13059-017-1382-0.

80. Andreatta, M., Hérault, L., Gueguen, P., Gfeller, D., Berenstein, A.J., and Carmona, S.J. (2024). Semi-supervised integration of single-cell transcriptomics data. Nat. Commun. *15*, 872. https://doi.org/10.1038/s41467-024-45240-z.

Please cite this article in press as: Lin et al., Tumor immune microenvironment remodeling predicts response to checkpoint inhibitor therapy, Cancer Cell (2026), https://doi.org/10.1016/j.ccell.2026.08.007

STAR★METHODS

KEY RESOURCES TABLE

REAGENT or RESOURCE	SOURCE	IDENTIFIER
Biological samples		
Human skin melanoma samples	University Hospital Essen	See Table S1 for details
Critical commercial assays		
Tumor Dissociation Kit, human	Miltenyi Biotec	Cat#130-095-929
Chromium Next GEM Single Cell 5′ Library & Gel Bead Kit v1.1	10× Genomics	Cat#1000165
Deposited data		
Raw sequencing data	This study	EGAS50000000459
Processed scRNA-seq and Visium data	This study	https://doi.org/10.5281/zenodo.19586163
Public human cancer scRNA-seq and Visium data	Othe public studies	See Table S2 for details
Public human cancer bulk transcriptomic data	Othe public studies	See Table S2 for details
Software and algorithms		
Cell Ranger 3.0.0	10× Genomics	https://10xgenomics.com/
Space Ranger 2.0.0	10× Genomics	https://10xgenomics.com/
R 4.5.2	R Core Team	https://www.r-project.org/
Python 3.10.16	Python Software Foundation	https://www.python.org/
Seurat 5.3.0	Hao et al.[68]	https://satijalab.org/seurat/
scDblFinder	Germain et al.[69]	https://github.com/plger/scDblFinder
DoubletFinder	McGinnis et al.[70]	https://github.com/chris-mcginnis-ucsf/DoubletFinder
SingleR 2.12.0	Aran et al.[39]	https://github.com/dviraran/singler
scGate 1.7.2	Andreatta et al.[40]	https://github.com/carmonalab/scGate
harmony 1.2.4	Korsunsky et al.[71]	https://github.com/immunogenomics/harmony
infercnv 1.26.0	Tickle et al.[72]	https://github.com/broadinstitute/infercnv
scCODA 0.1.9	Büttner et al.[41]	https://github.com/theislab/sccoda
rcompanion 2.5.2	Mangiafico[73]	https://CRAN.R-project.org/package=rcompanion
metafor 5.0	Viechtbauer et al.[74]	https://github.com/wviechtb/metafor
GSVA 2.4.8	Hänzelmann et al.[75]	https://github.com/rcastelo/GSVA
clusterProfiler 4.18.4	Wu et al.[76]	https://github.com/YuLab-SMU/clusterProfiler
cell2location	Kleshchevnikov et al.[77]	https://github.com/BayraktarLab/cell2location
CellChat	Jin et al.[78]	https://github.com/jinworks/CellChat
xCell2 1.2.3	Angel et al.[52]	https://github.com/AlmogAngel/xCell2
scanpy 1.12.1	Wolf et al.[79]	https://github.com/scverse/scanpy

EXPERIMENTAL MODEL AND STUDY PARTICIPANT DETAILS

Study participant details

Patients with advanced melanoma who were to receive immunotherapy with anti-PD-1 antibodies alone or in combination with anti-CTLA4 antibodies from Departments of Translational Skin Cancer Research and Dermatology were included in the study upon written informed consent (ethics vote numbers 16-6784-BO and 16-7097-BO). For further clinical information, please refer to Table S1.

METHOD DETAILS

Single-cell RNA-seq data generation

Tumor tissue biopsies from melanoma lesions were obtained on the day of therapy initiation (day 0) and 6–16 days thereafter (see Table S1). Fresh biopsies were immediately processed after excision. The generation of the single cell suspension was performed

Please cite this article in press as: Lin et al., Tumor immune microenvironment remodeling predicts response to checkpoint inhibitor therapy, Cancer Cell (2026), https://doi.org/10.1016/j.ccell.2026.08.007

according to the tumor dissociation protocol from Miltenyi Biotec (Bergisch Gladbach, Germany). Briefly, the tissue biopsy was cut into small cubes of 2 mm and then minced with the gentleMACS program "h_tumor_01" and two times "h_tumor_02" with 30 min incubation time after each mince. During the incubation, the sample was digested with an enzyme cocktail mix consisting of 200 μL Enzyme H, 100 μL Enzyme R and 25 μL Enzyme A (catalog #130-095-929 Miltenyi Biotec). The cell suspension was reconstituted in PBS with 0.05% BSA and washed two to three times, before passing through a 100 μm cell strainer. Subsequently, the cells were processed with the Single Cell 5′ Library & Gel Bead Kit v1.1 (catalog #1000165, 10xGenomics, Pleasanton, CA, USA) according to the manufacturer's protocol. As input for the 10× protocol, 10,000 cells from the single cell suspension were loaded at a concentration of 1000 cells/μL. The resulting gene expression library was sequenced at genomics core facility of German Cancer Center (DKFZ), Heidelberg, Germany. The sequencing data were aligned with the GRCh38 human reference genome and quantified using Cell Ranger (version 3.0, 10× Genomics Inc).

Spatial transcriptomic data generation

Formalin-fixed paraffin-embedded (FFPE) tissue sections (5 μm) were processed using the 10× Genomics Visium CytAssist Spatial Gene Expression for FFPE workflow (CG000520). Sections were deparaffinized, H&E-stained, imaged, and decrosslinked prior to probe hybridization and library preparation. Spatial gene expression libraries were generated using the Visium CytAssist Spatial Gene Expression Reagent Kits (10× Genomics) and sequenced on an Illumina NovaSeq 6000 platform with paired-end reads. Raw base call files were demultiplexed and converted to FASTQ format using spaceranger mkfastq pipeline, and subsequently processed using spaceranger count with the FFPE probe-based workflow (Space Ranger v2.0.0), which performed probe alignment to the human reference genome (GRCh38), spatial barcode assignment, and UMI counting. The resulting count matrices and spatial coordinates were used for downstream analyses.

Single-cell RNA-seq data curation and standardization

Through an extensive literature review up to Mar 2025, we identified public scRNA-seq datasets across multiple cancer types with a specific focus on samples collected at the baseline and after the initiation of the ICI therapy (see Table S2).

Acknowledging the diverse response metrics used across neoadjuvant scRNA-seq studies, including RECIST, pathological assessment, PSA tests, T cell expansion, and early radiological evaluations, we harmonized responder classification for comparative analysis. Patients were designated as responders if they met any of the following criteria: achieving a complete or major pathological response, demonstrating a complete or partial response by RECIST, or being a pathological non-responder who nonetheless showed a RECIST response. In cohorts where response was primarily assessed via T cell expansion or blood prostate-specific antigen (PSA) levels, the original study's classification was adopted. Notably, consistent with the threshold used in BRCA_Bassez cohort from the same group, for the HNSCC_Franken cohort, patients with >30 T cell expanded clonotypes were classified as responders.

Given the wide sampling interval spanning 7 to 121 days from the first dose of immunotherapy, all samples were classified as either baseline (pre-treatment) or treated (on/post-treatment) status.

Single-cell RNA-seq data preprocessing

Newly generated single-cell sequencing data were aligned with the GRCh38 human reference genome and quantified using Cell Ranger (version 3.0, 10× Genomics Inc). The quality of cells was assessed based on two metrics: (1) The number of detected genes per cell; and (2) The proportion of mitochondrial gene counts per cell. Specifically, cells with detected genes fewer than 400 or greater than 8000, and mitochondrial unique molecular identifier (UMI) count percentage larger than 20% were filtered out. The genes detected in more than 5 cells were retained. To remove the potential doublets, scDblFinder[69] and DoubletFinder[70] were used for each sequencing library with the expected doublet rate set to be 0.08, and cells identified as doublets by both methods were further filtered out. For each dataset, gene symbols were converted into a common dictionary with STACASstandardizeGeneSymbols().[80] After the initial quality control and cell annotation, sample-level quality control was applied to remove samples with fewer than 200 non-malignant cells.

Hierarchical cell annotation

The hierarchical annotation framework facilitates consensus and flexible cell type assignment at two levels, i.e., main cell types and fine-granular subtypes (See Figures 2A and S1B; Table S3).

First level annotation was performed within individual datasets. SingleR[39] with the BlueprintEncodeData[15,16] reference data was applied to predict cell types. The annotation was refined by scGate[40] with a pre-defined multi-classifier (TME_HiRes) and Seurat V5 Louvain clustering[68] (default resolution) on corrected embeddings by Harmony.[71] Cells labeled as 'multi-label' and clusters with gene expression from multiple cell lineages were identified as doublets. Due to the technical limitations of 10× sequencing, the neutrophils were also excluded from subsequent analysis. The raw annotation from this step was improved by the following level 2 annotation and the final cross-dataset integration. Malignant cells were identified based on inferred copy number aberration (CNA) by infercnv package (see **Malignant cell identification** section).

Second level annotations were designed to cater to various cellular lineages, and consisted of two primary steps, i.e., reference preparation and hierarchical annotation.

For reference preparation, reference data for T cells, NK cells, myeloid cells, and CAFs were retrieved from the pan-cancer atlas studies,[3,4,6,8,20,21] loaded in R as *SingleCellExperiment* objects, and processed individually. The objects were split by cancer type or cohort as lists, normalized with *logNormCounts*(), and further aggregated into pseudo-bulk samples *aggregateReference*() by the

Please cite this article in press as: Lin et al., Tumor immune microenvironment remodeling predicts response to checkpoint inhibitor therapy, Cancer Cell (2026), https://doi.org/10.1016/j.ccell.2026.08.007

fine-granular level labels from original studies. Additionally, to capture the diversity of main components, data for T cells, myeloid cells, and B lymphocytes were also aggregated at the broad level (e.g., $CD4^+$ T cells, $CD8^+$ T cells, cDC, macrophages, B cells, plasma cells) to ensure accurate reclassification. Due to the relatively lower abundance, the reference data of NK cells was aggregated only at the main level ($CD56^{high}CD16^{low}$, $CD56^{high}CD16^{high}$, and $CD56^{low}CD16^{high}$).

For hierarchical annotation, immune cells were initially re-classified into main cell types within each lineage by SingleR based on the pan-cancer reference at the main level. For the T and NK cell group, this included $CD4^+$ T cells, $CD8^+$ T cells, and NK cells. For the myeloid cells group, this included cDCs, monocytes, and macrophages. For the B lymphocytes, this included B cells, GC B cells, and plasma cells. Due to the distinct marker expression, the scGate was applied to separate cells from the T and NK cells group, with *KLRD1* and *NCAM1* served as positive markers, and CD3D as a negative marker for NK cells, and *CD3D*, *TRGC2*, *TRDV2*, *TRGV9*, *TRGV10*, and *TRDC* as positive markers, and CD8A and CD4 as negative markers for the gamma delta T cells (gdT). After separating the NK and gdT, the remaining $CD4^+/CD8^+$ T cells underwent further 'gating' by the generic CD4T and CD8T models from scGate. Cells with overlapped labels were identified by SingleR, based on an aggregated pan-cancer reference at the main level. Similar procedures of reassignment at the first level were conducted on myeloid cells and B cells. The immune cells were then classified within each main cell type by SingleR with pan-cancer multiple reference at the fine-granular level. Non-immune cells including endothelial cells and fibroblasts cells were annotated directly to the fine-granular level by using SingleR with corresponding reference. After prediction, the labels were adjusted according to the extensively updated markers.

Finally, as a manual adjustment and quality control step for the final annotation, we performed cross-dataset integration within each cell lineage by Seurat integration. This step not only adjusted the annotation at different levels but was also instrumental for excluding problematic clusters. Clusters with high expression of proliferation-associated genes, such as *MKI67* and *TOP2A* were identified as cycling cell states. Clusters with clear expression of gene markers from multiple cell lineages and with high expression of ribosomal genes were identified as doublets and low-quality cells then were removed.

Malignant cell identification

The malignant cells detection was performed by using the inferCNV[72] package patient by patient. This process infers large-scale chromosomal copy number variations (CNVs) from single-cell RNA-sequencing data. First, the data were subsetted by patient, including epithelial cells (which are considered the origin of the tumor), and a reference population of various non-malignant cell types like fibroblasts and monocytes. The CNV states were predicted with a three-state CNV model (HMM_type = 'i3'). Cells with both average proportion of CNV-affected chromosomes (proportion_cnv_avg) and the average number of CNV events (has_cnv_avg) above the 90th percentile were classified as malignant.

Cell type abundance

Cell type frequencies were computed as within-compartment proportions, where immune cell subtypes (T/NK cells, B/plasma cells, myeloid cells) were calculated relative to the total immune cell count, and non-immune cell subtypes (stromal, endothelial) were calculated relative to the total non-immune cell count. Malignant, epithelial, and melanocyte populations were omitted from all compositional analyses. Samples containing fewer than 50 immune cells or fewer than 100 non-malignant cells were excluded.

To track compositional dynamics across sequential treatment cycles, per-patient fold changes were computed as the ratio of the treated frequency to the baseline frequency, where a pseudocount of 0.001 was added to both the numerator and denominator to prevent division by zero. Median fold changes were subsequently derived for each cancer type and time point, with analyses restricted to groups containing a minimum of three patients.

Meta-analysis of inter-cohort compositional analysis

To assess the consistency of cell type abundance changes between baseline and on-treatment states while accounting for across-study variability, we conducted a two-stage meta-analysis framework combining within-cohort statistical testing with cross-cohort effect pooling.

First, within each cohort, the relative abundance of each cell type was compared between baseline and treated samples. For the overview of all major cell types, we applied the unpaired Wilcoxon rank-sum test using all available TME samples. For further analyses on non-malignant cell types, we applied paired Wilcoxon rank-sum test restricted to patients with matched baseline and on-treatment biopsies. In both cases, the effect size was quantified as the rank-biserial correlation (r). For unpaired comparisons, r and its 95% confidence interval were estimated via the wilcoxonRG function from the rcompanion R package with 1,000 bootstrap replicates (R = 1000, conf = 0.95), and the standard error was derived as $SE = \frac{CI^{upper} - CI^{lower}}{2} * 1.96$. For paired comparisons, r was calculated as the matched-pairs rank-biserial correlation, $r = 2 * \frac{V}{n} * (n + 1) - 0.5$, where V is the Wilcoxon rank-sum statistic and n is the number of matched pairs, with $SE = \sqrt{(1 - r^2)/(n - 2)}$. Cohort-cell type combinations with fewer than two samples per group (unpaired) or fewer than three matched pairs (paired) were excluded.

To validate the robustness of these findings under a compositional data framework, we performed an independent analysis using scCODA, which models cell type counts via a Bayesian Dirichlet-multinomial distribution with spike-and-slab priors, thereby accounting for the inherent compositionality of single-cell proportions. For each cohort, a scCODA model was fitted with treatment status as the covariate and automatic reference cell type selection. Posterior distributions were sampled via Hamiltonian Monte Carlo with 20,000 iterations (num_results = 20000) and 5,000 burn-in steps (num_burnin = 5000). Credible effects were identified at a false

Please cite this article in press as: Lin et al., Tumor immune microenvironment remodeling predicts response to checkpoint inhibitor therapy, Cancer Cell (2026), https://doi.org/10.1016/j.ccell.2026.08.007

discovery rate threshold of 0.3 (est_fdr = 0.3) based on cumulative inclusion probabilities. For each cohort-cell type combination, the posterior mean effect was computed as the midpoint of the 94% highest density interval (HDI, 3%–97%), and the posterior standard deviation served as the uncertainty estimate. Per-cohort scCODA results were subsequently subjected to the same cross-cohort meta-analysis procedure described below.

Second, to synthesize the within-cohort results across studies, we performed a random-effects meta-analysis for each cell type using the rma function from the metafor R package (method = "REML"). Per-cohort rank-biserial correlations (or scCODA posterior means for the compositional validation) served as the effect size estimates (yi), with their corresponding standard errors (sei) used for inverse-variance weighting. The restricted maximum likelihood (REML) estimator was applied to estimate the between-study heterogeneity variance (τ^2). For each cell type, the model yielded a pooled effect size with 95% confidence interval, a significance test p value, and heterogeneity statistics including I^2 (the percentage of total variability attributable to between-cohort heterogeneity) and τ^2. Cell types were included in the meta-analysis if at least two cohorts provided valid estimates.

Gene set enrichment analysis

Gene set enrichment for scoring at bulk (including pseudobulk) and single cell level was conducted by using ssGSEA method from GSVA package[75] and *AddModuleScore()* from Seurat,[68] individually.

Differential expression analysis and over-representation enrichment analysis

The differential expression (DE) analysis was performed by using *FindAllMarkers()* function from the Seruat package based on the Wilcoxon rank-sum test. Mitochondrial genes and ribosomal genes were removed before DE analysis. In pseudobulk DE analysis, minimum fraction of detection of 0.9 was added as filtering criteria. The functional enrichment analysis was performed by using the clusterProfiler R package.

Non-negative matrix factorization (NMF) analysis for identifying tissue-specific cellular programs

With the compositional data as matrix V (cell type $\times$ sample), we performed NMF by using R package NMF across samples from both pre- and on-treatment time points to identify tissue-specific programs within the TME. With n samples and m cell types, V is a non-negative matrix in $V \in R^{m \times n}$. Then V could be decomposed into 2 non-negative matrices: $W \in R^{m \times k}$ and $H \in R^{k \times n}$, where k represents the pre-selected factor number. Each element in W matrix indicates the loading of a cell type on a corresponding factor, while elements of H capture activity levels of these factor across tumor samples.

To assess the influence of the k parameter on NMF outcomes, we ran the NMF analysis on the immune matrix using a range of values for k (3–10), with 200 iterations for each value and a fixed seed. Following the guidelines suggested in the NMF vignette, we selected a factorization rank of 4 based on the following criteria: the first value where the cophenetic coefficient began to decrease after a high plateau, the rank exhibiting the highest dispersion value, and the rank at which the consensus silhouette score reached its peak. We considered each NMF factor to represent a distinct multicellular program. To identify the representative cell types associated with each program, we applied hierarchical clustering to the scaled Wmatrix.

To recover the NMF weights of these programs in validation samples, we used a custom NMF strategy that holds the pre-identified W matrix constant. This method initializes a new H matrix and iteratively updates it to find the best fit for the new data, minimizing the Euclidean distance between the new data matrix and the product of the fixed W and the new H. The resulting H matrix thus provides the weights levels of the four cellular programs for each sample.

Assignment of scRNA-seq and bulk transcriptomic data to TIME subtypes

The relative abundance of immune cells of tumors for in-house validation set were calculated as aforementioned. For bulk transcriptomic data, the TME components were estimated by ssGSEA with representative gene sets (see Table S6). Then, we scaled the query data of the validation cohort to the original data and computed the Spearman's correlation coefficient between the scaled proportions of each patient in the validation cohort and those in the original atlas. Each patient in the validation cohort was assigned to the group with the Spearman's correlation coefficient above 0.25 with the corresponding group in the original atlas.

Cell-cell interaction analysis

We applied CellChat v2.[78] to quantify the probability of signaling communication based on the expression of ligand-receptor pairs across cell types. CellChat employs the law of mass action to quantify communication probability and identify statistically significant interactions with permutation tests. To control for the false positivity, we further filtered the interaction detected in at least 1/3 tumors in each group.

Abundance estimation in spatial transcriptomic data

The 10$\times$ Visium transcriptional data were loaded as a scanpy[79] object and pre-processed with 200 count per spot threshold. The probability of fine-grained cell subtype for each spot was estimated by cell2location,[77] a Bayesian model for spatial cell type mapping. To reduce the variation and ensure the accuracy, we used the matched scRNA-seq data from the same cohort as reference.

Please cite this article in press as: Lin et al., Tumor immune microenvironment remodeling predicts response to checkpoint inhibitor therapy, Cancer Cell (2026), https://doi.org/10.1016/j.ccell.2026.08.007

Transition classification and comparison with B cell classifiers

Based on the observed association between TIME subtype transitions and treatment response, we classified transition patterns as response-favorable or response-unfavorable. The response-favorable category includes transitions from TIME-I to TIME-B or TIME-Q, from TIME-Q or TIME-Mye to TIME-I, and maintenance of TIME-B. The response-unfavorable category includes maintenance of TIME-Q, TIME-Mye, or TIME-I states, TIME-Q to TIME-Mye, and TIME-B to TIME-Q. Transitions not captured by either category were excluded from further classifier comparison, with definitions refined in subsequently cancer-type-specific analysis.

To evaluate whether the transition classification adds response-discriminative information beyond B cell abundance at treated status, we compared three binary classifiers: (i) transition status (favorable vs. unfavorable), (ii) treated B/plasma cell abundance (high vs. low, defined by median of the B and plasma cell abundance among immune cells in the treated sample), and (iii) treated TIME-B status (yes vs. no, based on the TIME subtype assignment of the treated sample). For the pooled analysis, response rates were compared using the Chi-square test. Cancer-type-adjusted odds ratios were estimated from logistic regression models. To formally test the added value of one classifier over another, nested models were compared using likelihood ratio tests: the improvement in model fit when adding transition status to a B cell-only model (and vice versa) was assessed by the chi-square distributed test statistic with one degree of freedom.

Development and evaluation of transition-associated signature

(1) Deriving transition gene signature.

To identify baseline molecular features predictive of favorable TIME remodeling under ICI therapy, we derived a transition signature from baseline scRNA-seq pseudobulk profiles and evaluated its predictive performance on independent bulk transcriptomic cohorts.

Immune pseudobulk expression profiles were generated by averaging gene expression across all immune cells (T/NK, B/plasma, and myeloid lineages) per sample using Seurat's *AggregateExpression* function. Based on the TIME subtype transition patterns described above, we defined transition labels for TIME-I and TIME-Mye independently. For baseline TIME-I (inflamed) tumors, samples transitioning to TIME-B or TIME-Q were labeled as favorable (response-associated), while those transitioning to TIME-Mye were labeled as unfavorable. For baseline TIME-Mye (myeloid-enriched) tumors, those transitioning to any other subtype (TIME-I, TIME-B, or TIME-Q) were labeled as favorable, and those remaining TIME-Mye were labeled as unfavorable. Baseline samples from labeled patients were included in the training sets.

Feature selection was performed separately for the TIME-I and TIME-Mye groups using a random forest (RF) stability selection procedure. For each group, the expression matrix was first filtered to the top 4,000 most variable genes. A total of 200 RF iterations were then executed in parallel, each fitting a classification model using the ranger R package (num.trees = 1000, importance = "permutation"). Class weights were applied to address sample imbalance, assigning a weight of n_favorable/n_unfavorable to unfavorable samples and a weight of 1 to favorable samples. At each iteration, the top 100 genes ranked by out-of-bag (OOB) permutation importance were recorded. Gene selection frequency was computed as the proportion of iterations in which each gene appeared among the top 100. The number of signature genes was determined by applying the Kneedle algorithm to the ranked frequency curve, identifying the elbow point (maximum perpendicular distance to the diagonal within a search range of 15–80 genes) where additional genes contributed diminishing discriminative value. Each selected gene was then assigned a direction (up or down) based on whether its mean expression was higher in the favorable or unfavorable group.

(2) Evaluating clinical relevance.

The final transition signature was constructed as the union of genes selected from the TIME-I and TIME-Mye analyses. For genes appearing in both sets, the direction was resolved using the higher importance weight. The combined signature was scored on bulk transcriptomic data using a directional single-sample gene set enrichment analysis (ssGSEA). To account for cohort-specific batch effects, scores were z-scored within each cohort prior to cross-cohort analyses. Predictive performance was assessed across three clinical endpoints: treatment response, progression-free survival (PFS), and overall survival (OS). For treatment response, per-cohort odds ratios (ORs) were estimated using logistic regression with the z-scored transition score as the predictor. Cohorts were included if they contained at least 15 samples with at least 3 responders and 3 non-responders. The pooled OR was estimated from a logistic regression model with cohort included as a covariate. For survival endpoints, per-cohort hazard ratios (HRs) were estimated using Cox proportional hazards models (survivalcoxph). Cohorts were included if they contained at least 15 samples and at least 5 events. Pooled HRs were estimated from Cox models with cohort as a fixed-effect covariate. All confidence intervals were computed at the 95% level via Wald-type approximation. For Kaplan-Meier analysis, transition signature scores were computed for each baseline sample and z-scored within each cohort. Patients were stratified into high (fourth quartile, Q4) and low (first quartile, Q1) groups based on within-cohort score distributions. Survival curves were estimated using the Kaplan-Meier method, and differences between groups were assessed using two-sided log rank test.

To benchmark the transition signature against established ICI response signatures, we computed 10-fold cross-validated AUROC using logistic regression with cohort adjustment, where predicted probabilities from held-out folds were aggregated to construct the receiver operating characteristic curve, with 95% confidence intervals obtained via 1,000 bootstrap replicates (see Figure S5).

Please cite this article in press as: Lin et al., Tumor immune microenvironment remodeling predicts response to checkpoint inhibitor therapy, Cancer Cell (2026), https://doi.org/10.1016/j.ccell.2026.08.007

QUANTIFICATION AND STATISTICAL ANALYSIS

All statistical analyses were performed in R (v4.5.2) and Python (v3.10.16). Two-sided tests were used throughout unless otherwise stated, and statistical significance was set at $p < 0.05$. In the boxplots, the upper whisker indicates the maximum value or 75th percentile +1.5 IQR; the lower whisker indicates the minimum value or 25th percentile −1.5 IQR. Detailed statistical methods for each analysis are described in the corresponding methods subsections above.